Cross-link RTS/CTS for MLO mm-Wave WLANs

Zhuoling Chen, Yi Zhong, *Senior Member, IEEE*, Martin Haenggi, *Fellow, IEEE*

***Abstract*—The directional RTS/CTS mechanism of mm-wave Wi-Fi hardly resolves the hidden terminal problem perfectly. This paper proposes cross-link RTS/CTS under multi-link operation (MLO) to address this problem and introduces a novel point process, named the generalized RTS/CTS hard-core process (G-HCP), to model the spatial transceiver relationships under the RTS/CTS mechanism, including the directional case and the omnidirectional case. Analytical expressions are derived for the intensity, the mean interference, an approximation of the success probability, and the expected number of hidden nodes for the directional RTS/CTS mechanism. Theoretical and numerical results demonstrate the performance difference between two RTS/CTS mechanisms. The cross-link RTS/CTS mechanism ensures higher link quality at the cost of reduced network throughput. In contrast, the directional RTS/CTS sacrifices the link quality for higher throughput. We further provide a quantitative evaluation of the additional overhead introduced by the cross-link RTS/CTS mechanism based on the existing Wi-Fi standards and introduce a hybrid RTS/CTS selection method. Our study reveals a fundamental trade-off between link reliability and network throughput, providing critical insights into the selection and optimization of RTS/CTS mechanisms in next-generation WLAN standards.**

***Index Terms*—millimeter wave, Wi-Fi, RTS/CTS mechanism, stochastic geometry**

I. Introduction

A. Motivations

Over the past decades, Wireless Local Area Network (WLAN) standards have evolved into one of the most widely adopted and efficient networking technologies. Among them, Wi-Fi has become the dominant solution for providing ubiquitous wireless connectivity. The first Wi-Fi standard, released by IEEE in 1997, enabled a maximum throughput of 2 Mbps [2], thereby formalizing WLAN technology in the 2.4 GHz band. However, such performance has quickly become inadequate to satisfy the rapidly growing demand for high-speed wireless access.

To meet these demands, subsequent Wi-Fi generations have continuously enhanced their physical (PHY) and medium access control (MAC) capabilities. Notable advances include the introduction of Orthogonal Frequency-Division Multiplexing (OFDM) in IEEE 802.11a (Wi-Fi 2) [3] and Orthogonal Frequency-Division Multiple Access (OFDMA) in IEEE 802.11ax (Wi-Fi 6), as well as the extension of usable spectrum resources [4]. In particular, Wi-Fi 6E further expanded into the 6 GHz band [5], while IEEE 802.11ad and 802.11ay pioneered the use of millimeter-wave (mm-wave) communications.

Despite these advances, mm-wave transmissions in IEEE 802.11ad/ay still suffer from several fundamental limitations, which have hindered their large-scale commercial deployment [6]. The fundamental propagation characteristics of 60 GHz mm-wave, including severe penetration losses and blockage sensitivity, fundamentally restrict the applicability. The communication relies on narrow directional beams for sufficient gain, but even slight terminal movement or obstruction can cause beam misalignment, leading to poor reliability in mobile scenarios. Moreover, the rigid and time-consuming Beamforming Training (BFT) process of 802.11ad/ay causes extremely high latency. The quasi-omni antenna configuration inherent to 802.11ad/ay's initial access mechanism frequently induces asymmetric links.

Along with the large-scale adoption of Wi-Fi [7], medium access coordination has emerged as a critical challenge. The hidden terminal problem, in particular, significantly degrades network performance. To mitigate this issue, IEEE introduced the Request-to-Send/Clear-to-Send (RTS/CTS) handshake [8]. In mm-wave systems, beamforming is widely employed to combat high-frequency propagation impairments [9]. However, the resulting directional transmissions render the conventional RTS/CTS mechanism less effective, as neighboring nodes outside the beam path may fail to detect control frames, thereby causing collisions (see Fig. 1).

To address these limitations, the IEEE 802.11be standard (Wi-Fi 7) has recently introduced multi-link operation (MLO), which allows simultaneous use of both sub-7 GHz and mm-wave links [10]–[12]. This integration provides new opportunities to enhance MAC-layer coordination in next-generation mm-wave Wi-Fi, where the mm-wave link is just used for high-throughput data delivery with one or more dedicated sub-7 GHz links for control. Motivated by this, we propose a novel *cross-link RTS/CTS mechanism* that leverages the sub-7 GHz band for control frame exchange while maintaining mm-wave transmissions for high-rate data (see Fig. 2). Specifically, RTS and CTS frames are transmitted in the sub-7 GHz band so that neighboring devices, regardless of beam orientation, can correctly update their Network Allocation Vector (NAV) and avoid collisions in the mm-wave band. Furthermore, the proposed mechanism can just be interpreted as a reliability transmission solution for next-generation mm-wave Wi-Fi in the scenarios, where the mm-wave link suffers from severe hidden-node collisions due to directional transmission, rather than replacing the initial design goal of MLO, simultaneous multi-link payload transmission.

This work is thus motivated by the necessity to systematically model and analyze the spatial characteristics of both the conventional directional RTS/CTS and the proposed cross-link

Zhuoling Chen and Yi Zhong are with the School of Electron. Inf. & Commun., Huazhong University of Science and Technology, Wuhan, China. Martin Haenggi is with the Dept. of Electrical Engineering, University of Notre Dame, US. The research has been supported by the National Natural Science Foundation of China (NSFC) grant No. 62471193. Preliminary findings of this work were presented in the 23rd International Symposium on Modeling and Optimization in Mobile, Ad Hoc, and Wireless Networks (WiOpt 2025) [1].

The corresponding author is Yi Zhong (yzhong@hust.edu.cn).

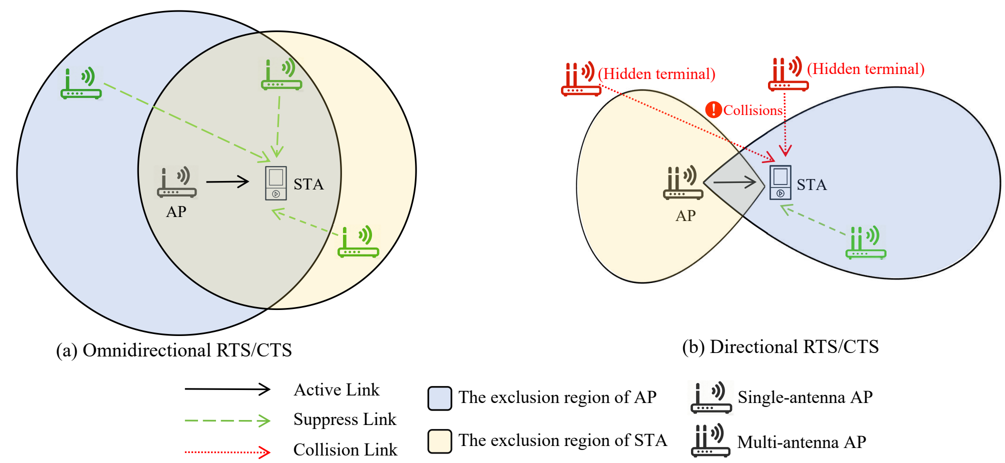

Fig. 1. Illustration of the hidden terminal problem under omnidirectional and directional RTS/CTS mechanisms. Three types of APs are shown: (i) black APs that are actively communicating with their associated Stations (STAs), (ii) green APs that are silenced by the RTS/CTS mechanism and thus prohibited from transmitting, and (iii) the remaining APs that act as hidden terminals and may cause collisions. In the omnidirectional case, nearby APs detect the RTS/CTS frames and defer transmissions. In the directional case, the beamformed transmission prevents AP1 and AP2 from overhearing the RTS/CTS frames, even though they are located near the STA. As a result, AP1 and AP2 may initiate transmissions during the ongoing communication, leading to collisions.

RTS/CTS mechanisms. By providing rigorous performance benchmarks, we aim to guide the design and optimization of next-generation WLAN protocols that integrate sub-7 GHz and mm-wave technologies under the MLO framework.

B. Related Work

The MLO framework in Wi-Fi 7 (IEEE 802.11be) represents a fundamental architectural milestone for future mm-wave WLANs. By integrating sub-7 GHz and mm-wave technologies, MLO enables next-generation wireless applications with higher throughput, lower latency, and enhanced reliability [13]. Building upon this vision, the Integrated Millimeter Wave (IMMW) Study Group has proposed a Project Authorization Request (PAR) [14], which defines a new standard, IEEE 802.11bq, aimed at extending the reuse of sub-7 GHz PHY/MAC specifications to the mm-wave band under the 802.11be MLO framework. Despite these advances, the design of a robust RTS/CTS handshake mechanism tailored for integrated sub-7 GHz and mm-wave systems remains largely unexplored in the current literature.

In parallel, extensive research has been devoted to characterizing mm-wave networks through both empirical measurements and theoretical models [15]–[20]. For instance, [16] employs stochastic geometry to analyze mm-wave networks within finite regions using a tractable flat-top antenna pattern. While analytically convenient, the flat-top model introduces inaccuracies in evaluating transmission success probabilities. To mitigate this issue, [20] proposes sinc and cosine antenna patterns, which significantly improve approximation accuracy and enable more precise derivations of network success probability. However, these models are predominantly developed under the assumption of a Poisson point process (PPP), which is poorly aligned with networks governed by RTS/CTS protocols.

To address this discrepancy, traditional hard-core point processes, such as the Matérn hard-core model [21]–[23], have been adopted to study CSMA-based networks. [23] derive closed-form analytical expressions for crucial network performance metrics based on the type II Matérn hard-core model. Yet, these models fall short of capturing the unique characteristics of RTS/CTS-enabled networks, where both transmitters and receivers enforce exclusion regions. To overcome this limitation, [24] introduces the dual-zone hard-core process (DZHCP), which explicitly incorporates dual exclusion regions around transmitters and receivers. Although promising, the DZHCP framework is currently limited to omnidirectional antenna scenarios and cannot accurately model directional RTS/CTS mechanisms in mm-wave networks.

Another line of research focuses on the analytical tractability of the success probability in hard-core point processes, which is intractable in closed form. The work in [25] derives an analytical bound under the densely packed assumption. To overcome this limitation, several studies have developed the Approximate SIR Analysis based on the PPP (ASAPPP) framework [26]–[28], which enables tractable approximations while preserving key spatial correlations. Initially developed for cellular models, ASAPPP provides accurate approximations by mapping hard-core processes onto PPP-based equivalents. More recently, [24] extended the applicability of ASAPPP to bipolar models and demonstrated its validity in this broader context. Nonetheless, most existing studies employing ASAPPP or related methods remain focused on sub-7 GHz networks, typically assuming Rayleigh fading, which limits their applicability to directional mm-wave scenarios with RTS/CTS mechanisms.

C. Contributions

This paper focuses on the two types of RTS/CTS handshake mechanism. We investigate the mean interference and the approximate success probability in mm-wave networks with the blockage effect reflected by a LOS ball blockage model under the RTS/CTS handshake mechanism. The key contributions of our study are summarized as follows:

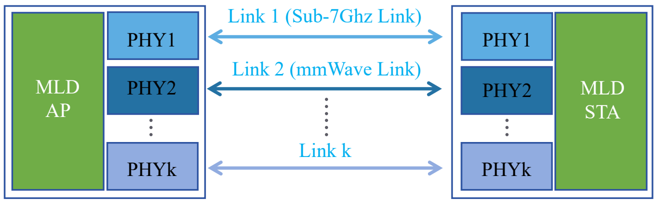

Fig. 2. Illustration of the mm-wave Wi-Fi supporting MLO. This mm-wave Wi-Fi devices are equipped with multiple independent physical layer for each link, enabling simultaneous communication on different frequency bands or channels. The connection between AP and STA includes multiple links including at least one link in the sub-7 GHz band and another in the mm-wave band. If there is any blockage in the mm-wave link, the sub-7 GHz link can ensure communication quality.

- We propose a novel exclusion region model based on cosine antenna patterns, applicable to both directional and omnidirectional scenarios. Based on the exclusion region, we introduce a novel hard-core point process, named generalized RTS/CTS hard-core process (G-HCP), to characterize the spatial properties of directional RTS/CTS mechanism and the cross-link RTS/CTS mechanism.
- Leveraging classical statistical measures and analytical tools, we derive the expressions for mean interference. Besides, We extend the ASAPPP method to approximate the success probability under integer-parameter Nakagami-M fading channels, accounting for a finite LOS communication region. An exact expression for the mean interference-to-signal ratio (MISR) in a bounded domain is established to support this approximation.
- In the context of directional RTS/CTS, we provide an exact expression for the expected number of hidden nodes, revealing the impact of system parameters such as antenna array size, frequency, and node density.
- We provide a quantitative evaluation of the additional overhead introduced by the cross-link RTS/CTS mechanism, and we introduce the reservation inefficiency ratio to reflect the spectrum-utilization inefficiency of sub-7 GHz.

II. Stochastic Model for RTS/CTS-Enabled Networks

A. Network and Channel Assumptions

We consider a MLD network where each transceiver can operate simultaneously in the sub-7 GHz and mm-wave bands. All devices employ a single omnidirectional antenna for sub-7 GHz communications, while the mm-wave transmission relies on uniform linear arrays (ULAs) with N_t (for MLD transmitters) and N_r (for MLD receivers) antenna elements. The mm-wave reception is omnidirectional. Omnidirectional transmission is restricted to the sub-7 GHz band and is triggered only when (i) the cross-link RTS/CTS mechanism is enabled, and (ii) the transmitted frame is a cross-link RTS or CTS frame. For all other cases, mm-wave directional transmission is applied, whereas reception remains omnidirectional.

We assume the omnidirectional reception to simplify spatial analysis. Although directional reception can suppress interference from certain directions, it also changes the CTS clear region and the geometric distribution of hidden nodes. Accordingly, directional receive beamforming will lead to different quantitative results. However, the fundamental trade-off, where directional RTS/CTS provides higher spatial reuse but is more vulnerable to hidden nodes while cross-link RTS/CTS improves reliability at the cost of additional overhead, remains unchanged.

Blockage is modeled using the LOS ball model [15], with LOS radius R representing the maximum distance within which potential LOS interferers exist. Given that NLOS paths are typically over 20 dB weaker than LOS paths [29], we restrict our analysis to LOS channels. The mm-wave propagation follows a clustered channel model, where the channel vector between transmitter y and its receiver is given by

$$\mathbf{h}_y = \sqrt{N_\mathrm{t}}\rho_y \mathbf{a}_\mathrm{t}^H(\vartheta_y), \tag{1}$$

with fading coefficient ρ_y modeled as Nakagami-M, and $\mathbf{a}_\mathrm{t}(\vartheta_y)$ is the array response vector as

$$\mathbf{a}_\mathrm{t}(\vartheta_y) = \frac{1}{\sqrt{N_\mathrm{t}}}\left[1, \cdots, e^{j2\pi k\vartheta_y}, \cdots, e^{j2\pi(N_\mathrm{t}-1)\vartheta_y}\right]^T, \tag{2}$$

where $\vartheta_y = \frac{d_0}{\lambda}\sin\phi_y$, and d_0, λ, and ϕ_y represent the antenna spacing, wavelength, and physical angle of departure (AoD).

The optimal analog beamforming vector between transmitter y and its intended receiver is

$$\mathbf{w}_y = \mathbf{a}_\mathrm{t}(\varphi_y), \tag{3}$$

yielding the beamforming gain

$$G_\mathrm{act}(\vartheta_y - \varphi_y) = \left|\mathbf{a}_\mathrm{t}^H(\vartheta_y)\mathbf{w}_y\right|^2 = \frac{\sin^2(\pi N_\mathrm{t}(\vartheta_y - \varphi_y))}{N_\mathrm{t}^2 \sin^2(\pi(\vartheta_y - \varphi_y))}. \tag{4}$$

For tractability, we approximate this gain by a cosine antenna pattern [20] in (8).

The perfect beam alignment assumption corresponds to a best beam training condition, where the intended transmitter and receiver have already established their dominant beam directions. This assumption allows us to isolate the hidden-node effect from beam training errors and improve analytical tractability. In practical mobile scenarios, beam alignment suffers from many factors, such as terminal rotation, and dynamic blockage and so on. Therefore, the results for directional RTS/CTS can be regarded as a best case of the beam training of the mm-wave control frame, which means the analytical results in this paper are intended to provide qualitative insights into the system level rather than serve as exact quantitative predictions for a fully realistic mm-wave PHY.

B. Generalized RTS/CTS Hard-Core Process

We model the locations of transceivers using a Poisson bipolar process, where the transmitters are distributed according to a homogeneous PPP, each paired with a receiver at a fixed distance d and a uniformly random angle θ. The RTS/CTS mechanism is incorporated through a thinning procedure, which selectively removes transceiver pairs from the underlying process based on the RTS/CTS handshake rules. This allows us to capture both the directional RTS/CTS and the cross-link RTS/CTS in a unified framework.

The RTS/CTS operation induces exclusion regions around each transceiver pair, which consist of an RTS-cleaned region and a CTS-cleaned region. For omnidirectional RTS/CTS, the exclusion regions are isotropic, whereas directional RTS/CTS generates anisotropic exclusion regions due to beamforming.

We distinguish between two types of RTS/CTS thinning:

- *Type I thinning*: A transceiver pair is retained only if no other potential transmitter lies within its exclusion region. This corresponds to a synchronous channel access model where time is slotted and only one pair can be active within a given exclusion region. Collisions occur if multiple transmitters attempt to access the channel simultaneously.

- *Type II thinning*: Each transceiver is assigned a random time mark representing its channel access attempt. A transceiver is retained if no other transmitter with a smaller time mark lies within its exclusion region. This model reflects asynchronous contention, where multiple transceivers may coexist in a slot but priority is given to those with earlier access marks.

Both thinning schemes ensure that retained transceivers respect the RTS/CTS exclusion principle, with Type I emphasizing strict mutual exclusion and Type II offering a more realistic representation of distributed channel access.

To characterize the antenna effect, we approximate the actual beam pattern. For simplicity, we assume that the AoD between each transmitter and its associated receiver is zero, so the optimal analog beamforming vector reduces to

$$\mathbf{w}_y = \frac{1}{\sqrt{N_\mathrm{t}}}\,[1, 1, \ldots, 1]^T\,. \tag{5}$$

The corresponding beamforming gain is

$$G_{\mathrm{act}}(\vartheta_y) = \left|\mathbf{a}_\mathrm{t}^H(\vartheta_y)\mathbf{w}_y\right|^2 = \frac{\sin^2(\pi N_\mathrm{t}\vartheta_y)}{N_\mathrm{t}^2\sin^2(\pi\vartheta_y)}. \tag{6}$$

Following [20], we approximate this beamforming gain by the cosine model

$$G_{\cos}(\vartheta) = \begin{cases}\cos^2\left(\frac{\pi N_\mathrm{t}}{2}\vartheta\right), & |\vartheta| \le \frac{1}{N_\mathrm{t}},\\ 0, & \text{otherwise},\end{cases} \tag{7}$$

where $\vartheta = \frac{d_0}{\lambda}\sin\phi$.

Using the small-angle approximation $\sin(x) \approx x$ for small x, we further obtain a simplified directional gain

$$G_\mathrm{t}(\phi) = \begin{cases}\cos^2\left(\frac{\pi N_\mathrm{t} d_0}{2\lambda}\phi\right), & |\phi| \le \frac{\lambda}{d_0 N_\mathrm{t}},\\ 0, & \text{otherwise}.\end{cases} \tag{8}$$

In Fig. 3, we observe that the simplified gain provides a good approximation for the cosine gain. Based on the simplified gain, we define the RTS/CTS exclusion regions. For transmitter y and its receiver x, the RTS exclusion region is

$$S_{\mathrm{vs}}(y) \triangleq \Bigg\{ z \in \mathbb{R}^2 \mid \|\overrightarrow{yz}\| \le R_{\mathrm{vs}}\sqrt{G_\mathrm{t}(\phi)},\; \cos\phi = \frac{\overrightarrow{yz}\cdot\overrightarrow{yx}}{\|\overrightarrow{yz}\|\|\overrightarrow{yx}\|} \Bigg\}, \tag{9}$$

while the CTS exclusion region is

$$S_\mathrm{r}(x) \triangleq \left\{ z \in \mathbb{R}^2 \mid \|\overrightarrow{xz}\| \le R_\mathrm{r}\sqrt{G_\mathrm{r}(\phi)}, \cos\phi = \frac{\overrightarrow{xz}\cdot\overrightarrow{xy}}{\|\overrightarrow{xz}\|\|\overrightarrow{xy}\|} \right\}, \tag{10}$$

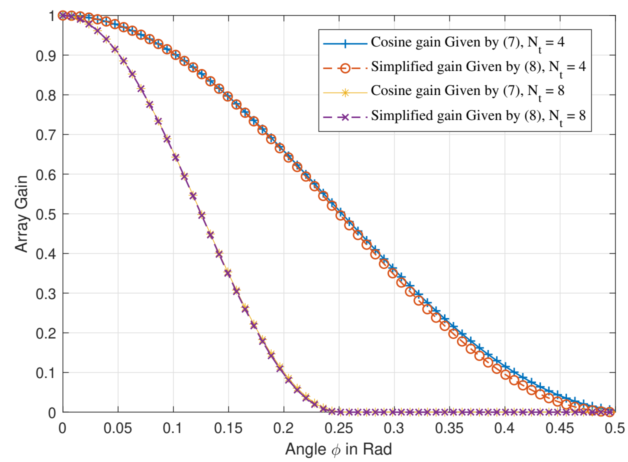

Fig. 3. The comparisons between the different gains.

with the receiver gain

$$G_\mathrm{r}(\phi) = \begin{cases}\cos^2\left(\frac{\pi N_\mathrm{r} d_0}{2\lambda}\phi\right), & |\phi| \le \frac{\lambda}{d_0 N_\mathrm{r}},\\ 0, & \text{otherwise}.\end{cases} \tag{11}$$

Here, R_{vs} and R_r denote the maximum transmission ranges of RTS and CTS frames. All transmitters follow the Carrier Sense Multiple Access with Collision Avoidance (CSMA/CA) protocol. Therefore, the exclusion of each transmitter consists of two regions: a physical carrier sensing (PCS) region caused by CSMA/CA protocol and a virtual carrier sensing (VCS) region, i.e., the RTS exclusion region. The PCS region exhibits a geometric shape consistent with that of the VCS region, but while a larger range, i.e., $R_\mathrm{t} > R_{\mathrm{vs}}$, where R_t denotes the maximum ranges of the PCS region, and the exclusion region of transmitter y is

$$S_\mathrm{t}(y) \triangleq \left\{ z \in \mathbb{R}^2 \mid \|\overrightarrow{yz}\| \le R_\mathrm{t}\sqrt{G_\mathrm{t}(\phi)},\; \cos\phi = \frac{\overrightarrow{yz}\cdot\overrightarrow{yx}}{\|\overrightarrow{yz}\|\|\overrightarrow{yx}\|} \right\}. \tag{12}$$

Therefore, the exclusion region of the transceiver pair with transmitter y and receiver x is

$$S(y, x) = S_\mathrm{t}(y) \cup S_\mathrm{r}(x). \tag{13}$$

When the antenna spacing is 0, $d_0 = 0$, all antennas can be regarded as a single antenna, which corresponds to the omnidirectional case. In this special case, the numbers of antennas (N_t and N_r) represent how many times larger the transmit power is compared to the per-antenna transmission power in the directional case, and both $S_\mathrm{t}(y, x)$ and $S_\mathrm{r}(y, x)$ reduce to disks centered at y and x, respectively. Therefore, the proposed exclusion region framework generalizes naturally to both omnidirectional (cross-link RTS/CTS) and directional RTS/CTS mechanisms, enabling a unified spatial model.

The simplified cosine antenna pattern is adopted to obtain tractable exclusion regions and analytically manageable expressions. This approximation captures the main dependence of beamwidth and main-lobe gain on the antenna array size, but it does not fully represent practical side lobes, irregular beam shapes. More realistic antenna patterns may change the exact numerical values of the interference, success probability,

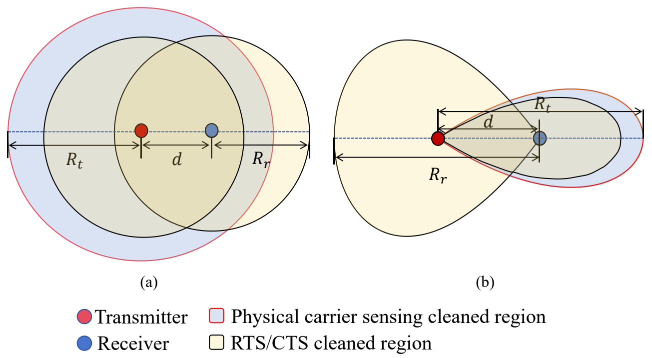

Fig. 4. Illustration of the exclusion region. (a) is the case of omnidirectional case, i.e., the cross-link RTS/CTS mechanism. (b) is the case of directional case with N_r=16 and N_r=8. The exclusion region consists of two parts, i.e. the physical carrier sensing cleaned region and the RTS/CTS cleaned region.

and hidden-node count. Nevertheless, the qualitative conclusion remains that directional RTS/CTS creates the anisotropic exclusion regions and may cause the hidden-node problem, whereas cross-link RTS/CTS provides a more isotropic reservation region through sub-7 GHz control signaling.

C. Mathematical Description

The G-HCP model employs a dependently marked PPP, denoted as $\widetilde{\Phi}_{\mathrm{PPP}}$, for the spatial distribution of the transmitters. This process is structured as follows:

- $\Phi_{\mathrm{PPP}} = \{y_i\} \subset \mathbb{R}^2$ denotes the locations of potential transmitters modeled by a PPP with intensity λ_p;
- x_i denotes the location of the receiver. θ_i is an i.i.d. orientation of the receiver x_i for the transmitter y_i, uniformly distributed in $[0, 2\pi]$. Having assumed a constant distance of d between a transmitter and its receiver, the orientation θ_i together with y_i uniquely determines the receiver x_i. These marks determine the time order of transmissions for each transmitter;
- e_i is the medium access indicator. Each transceiver pair (y_i, x_i) has a medium access indicator, which determines whether the transmitter could transmit.

1) Type I G-HCP: For the Type I G-HCP, let $\mathcal{N}(y, x, e)$ denotes the other transmitters within the exclusion region of transceiver pair (y, x):

$$\mathcal{N}(y,x,e) \triangleq \big\{(y',x',e') \in \widetilde{\Phi}_{\mathrm{PPP}} \setminus \{(y,x,e)\} : y' \in S_{\mathrm{t}}(y) \cup S_{\mathrm{r}}(x)\big\}. \tag{14}$$

The medium access indicator e_i is a dependent mark as

$$e_i = \mathbb{1}(\#\mathcal{N}(y_i, x_i, e_i) = 0), \tag{15}$$

where $\#$ denotes the count of elements in the neighborhood.

The set of transceiver pairs that have passed all RTS/CTS contention requirements, is denoted by $\tilde{\Phi}$

$$\tilde{\Phi} \triangleq \{(y, x, e) \in \tilde{\Phi}_{\mathrm{PPP}} \colon e = 1\}. \tag{16}$$

Finally, the set of active transmitters is defined as Φ

$$\Phi \triangleq \{(y, x, e) \in \tilde{\Phi} \colon y\} \tag{17}$$

2) Type II G-HCP: The difference between the Type I and the Type II is the time mark t, which reflects the time cost of a transmitter competing for channel access in the Type II.

- t_i is an i.i.d. time mark uniformly distributed in $[0, 1]$, representing the time cost of a transmitter competing for channel access, i.e., the relative initiation time of transmission for each transmitter.

For the Type II G-HCP, let $\mathcal{N}(y, x, t, e)$ be the neighborhood of the transmitters, which have smaller time marks than t and are within the exclusion region of transceiver pair (y, x).

$$\mathcal{N}(y,x,t,e) \triangleq \big\{(y',x',t',e') : (y',x',e') \in \widetilde{\Phi}_{\mathrm{PPP}} \setminus \{(y,x,e)\}, y' \in S_{\mathrm{t}}(y) \cup S_{\mathrm{r}}(x), t' < t\big\}. \tag{18}$$

The medium access indicator e_i of (y_i, x_i, t_i, e_i) is a dependent mark defined as

$$e_i = \mathbb{1}(\#\mathcal{N}(y_i, x_i, t_i, e_i) = 0). \tag{19}$$

The set of transceiver pairs that have passed all RTS/CTS contention requirements, is denoted by

$$\tilde{\Phi} \triangleq \{(y, x, e, t) \in \tilde{\Phi}_{\mathrm{PPP}} \colon e = 1\}. \tag{20}$$

Finally, the set of active transmitters is defined as Φ

$$\Phi \triangleq \{(y, x, e, t) \in \tilde{\Phi} \colon y\} \tag{21}$$

The G-HCP is used to describe the spatial distribution of the active transmitters within a time slot. Φ_{PPP} is the set of the locations of the transmitters that attempt to transmit within this time slot, which means Φ_{PPP} is reallocated within each slot. For the Type II G-HCP, the time marks are redrawn within each slot. Consequently, in both Type I G-HCP and Type II G-HCP, a transmitter's suppression is a temporary state per slot, not a permanent condition.

III. Network Performance Analysis

In this section, we analyze the network performance based on the proposed G-HCP model. Without loss of generality, we consider the typical transmitter y_o located at the origin o and its associated receiver x_o positioned at $(d, 0)$. To facilitate the derivations, we define several key quantities as follows

- Transceiver pair parameters (r, β, θ): each transceiver pair is represented by (r, β, θ), where the transmitter and receiver are located at $y = (r\cos\beta, r\sin\beta)$ and $x = (r\cos\beta + d\cos\theta, r\sin\beta + d\sin\theta)$, respectively.
- Union exclusion region $V(r, \beta, \theta)$: the spatial region covered by the union of the exclusion zones of the typical transceiver and a transceiver at (r, β, θ).
- Spatial criteria for interference S_1, S_2, S_3 and S_4: Define the spatial criteria for transmitters within the exclusion regions, helping to determine interference conditions:
  - $S_1 = \{(r, \beta, \theta) : r^2 \le R_{\mathrm{t}}^2 G_{\mathrm{t}}(\theta - \beta - \pi)\}$,
  - $S_2 = \{(r, \beta, \theta) : r^2 + 2rd\cos(\beta - \theta) + d^2 \le R_{\mathrm{r}}^2 G_{\mathrm{r}}(\arccos\frac{-r\cos(\theta-\beta)-d}{\sqrt{r^2+2rd\cos(\beta-\theta)+d^2}})\}$,
  - $S_3 = \{(r, \beta, \theta) : r^2 \le R_{\mathrm{t}}^2 G_{\mathrm{t}}(\beta)\}$,
  - $S_4 = \{(r, \beta, \theta) : r^2 - 2rd\cos\beta + d^2 \le R_{\mathrm{r}}^2 G_{\mathrm{r}}(\arccos\frac{r\cos\beta - d}{\sqrt{r^2-2rd\cos\beta+d^2}})\}$,

The set S_1 includes (r,β,θ) where o is within its transmitter's exclusion region. The set S_2 includes (r,β,θ) where o is within its receiver's exclusion region. The set S_3 includes (r,β,θ) of which the transmitter is within $S_{\rm t}(o)$. The set S_4 includes (r,β,θ) of which the transmitter is within $S_{\rm r}(x_o)$.

A. Node Intensity

In the G-HCP model, the point process Φ is obtained through a dependent thinning of the original PPP $\Phi_{\rm PPP}$. Under the Palm probability measure $\mathbb{P}^{\Phi_{\rm PPP}}$, the node intensity of the retained process $\Phi_{\rm PPP}$ can be expressed as

$$\lambda_b = \lambda_p\, \mathbb{P}^{\Phi_{\rm PPP}}(o \text{ retained}), \tag{22}$$

where $\mathbb{P}^{\Phi_{\rm PPP}}(\text{node retained})$ denotes the mean retention probability of a node in $\Phi_{\rm PPP}$ after applying the thinning rule.

1) Type I G-HCP: In the Type I G-HCP, a node is retained only if its exclusion region is free of any other nodes from Φ_a. This implies that each retained node corresponds to an empty exclusion zone. Consequently, the retention probability equals the void probability of a PPP with intensity λ_p, i.e.,

$$\mathbb{P}^{\Phi_{\rm PPP}}(o \text{ retained}) = \exp(-\lambda_p V_o), \tag{23}$$

where V_o is the area of the exclusion region associated with the typical node. Hence, the resulting node intensity is

$$\lambda_b = \lambda_p e^{-\lambda_p V_o}. \tag{24}$$

When the parent intensity λ_p is small, the retained intensity λ_b increases approximately linearly with λ_p. However, as λ_p becomes large, the exponential term dominates, leading to a decrease in λ_b. Therefore, λ_b reaches its maximum value at $\lambda_p = 1/V_o$, beyond which it monotonically decreases due to the exponential decay of $\mathbb{P}^{\Phi_{\rm PPP}}(o \text{ retained})$.

2) Type II G-HCP: In the Type II G-HCP, each transceiver pair is associated with a time mark $t \in [0,1]$, drawn independently from a uniform distribution. The time mark determines the priority of a node during the contention process. Specifically, a transmitter y with time mark t is retained only if no other transmitters with smaller time marks are located within its exclusion region. The overall node intensity is obtained as

$$\lambda_b = \lambda_p \int_0^1 e^{-\lambda_p t V_o}\, \mathrm{d}t = \frac{1}{V_o}\big(1 - e^{-\lambda_p V_o}\big). \tag{25}$$

It can be seen from (25) that λ_b is a monotonically increasing function of λ_p, asymptotically approaching its upper limit of $1/V_o$ as $\lambda_p \to \infty$.

B. Mean Interference

In this part, we will derive the mean interference at the typical transceiver pair in G-HCP.

The aggregate interference at the receiver x_o is

$$\mathrm{I}_{x_o} = \sum_{y\in\Phi\setminus\{o\}} P_0 N_{\rm t} |\rho_y|^2 G_{\rm t}\, l(\|y-x_o\|), \tag{26}$$

where P_0 is the per-antenna transmit power, the channel gain $|\rho_y|^2$ follows a gamma distribution $\mathrm{Gamma}(M, \frac{1}{M})$ and $l(\cdot)$ is the path-loss function.

Firstly, we derive the mean interference in the network, where all interferers are LOS interferers. The mean interference for the dual zone hard-core point process has been established in [24]. Building upon this result, we extend the derivation to obtain the mean interference for the directional RTS/CTS modeled by G-HCP.

Theorem 1. *The mean interference I_{x_o} experienced by the typical receiver x_o in G-HCP, under the assumption that all interferers are LOS interferers, is*

$$\mathbb{E}^!_{(o,0)}\left[I_{x_o}\right] = \frac{\lambda_p^2 P_0 N_{\rm t}}{2\pi\lambda_b} \int_0^\infty \int_0^{2\pi} \int_0^{2\pi} l\left(\sqrt{r^2 - 2rd\cos\beta + d^2}\right) G_{\rm t}(r,\beta,\theta) k(r,\beta,\theta) r \mathrm{d}\theta \mathrm{d}\beta \mathrm{d}r, \tag{27}$$

where $k(r,\beta,\theta)$ for the Type I process is

$$k(r,\beta,\theta) = \begin{cases} 0 & \text{if}(r,\beta,\theta) \in (S_1\cup S_2)\cup(S_3\cup S_4), \\ \exp\left(-\lambda_p V(r,\beta,\theta)\right) & \text{otherwise,} \end{cases} \tag{28}$$

and $k(r,\beta,\theta)$ for the Type II process is

$$k(r,\beta,\theta) = \begin{cases} 0 & (r,\beta,\theta) \in (S_1\cup S_2)\cap(S_3\cup S_4), \\ 2p(V) & (r,\beta,\theta) \in \overline{S_1}\cap\overline{S_2}\cap\overline{S_3}\cap\overline{S_4}, \\ p(V) & \text{otherwise,} \end{cases} \tag{29}$$

in which V is the abbreviation of $V(r,\beta,\theta)$, and $p(V)$ is

$$p(V) = \frac{V_o e^{-\lambda_p V} - V e^{-\lambda_p V_o} + V - V_o}{\lambda_p^2 (V - V_o) V V_o}. \tag{30}$$

Proof. Following the derivation in [24], under the reduced Palm probability and $\mathbb{E}[|\rho_y|^2] = 1$, (26) can be written as

$$\mathbb{E}^!_{(o,0)}[I_{x_o}] = \lambda_b P_0 N_{\rm t} \int_{\mathbb{R}^2\times[0,2\pi]} l(\|y-x_o\|) G_t(y,\theta)\, K_{(o,0)}(d(y,\theta)). \tag{31}$$

where $K_{(o,0)}(\cdot)$ is the reduced second-order factorial measure. Using the same argument as in [24], $K_{(o,0)}$ is related to the second-order product density, which can be expressed through the joint retention probability $k(y,\theta)$. Hence,

$$\mathbb{E}^!_{(o,0)}[I_{x_o}] = \frac{\lambda_p^2 P_0 N_{\rm t}}{2\pi\lambda_b} \int_{\mathbb{R}^2\times[0,2\pi]} l(\|y-x_0\|) G_t(y,\theta) k(y,\theta)\, d(y,\theta). \tag{32}$$

Finally, expressing y in polar coordinates as (r,β) and noting that

$$\|y - x_o\| = \sqrt{r^2 - 2rd\cos\beta + d^2}. \tag{33}$$

We obtain (27). Therefore, compared with [24], the only modification is that the product $l(\cdot)G_t(r,\beta,\theta)$ is treated as an equivalent path loss. □

Theorem 1 assumes that all interferers are LOS interferers. However, this leads to an over-estimation of the interference since, per our model, some paths are NLOS. A more accurate result is obtained by ignoring the interference along NLOS paths, which is significantly weaker than that along LOS paths.

Under this simplification, the mean interference in the LOS ball model can be derived using Theorem 1.

Corollary 1. *The mean interference $I_{x_o,R}$ experienced by the typical receiver x_0 in G-HCP with a LOS radius R is*

$$\mathbb{E}^!_{(o,0)}\left[I_{x_o,R}\right]=\frac{\lambda_p^2P_0N_\mathrm{t}}{2\pi\lambda_b}\int_0^{2\pi}\int_0^{2\pi}\int_0^{\sqrt{R^2-(d\sin\beta)^2}+d\cos\beta} l\left(\sqrt{r^2-2rd\cos\beta+d^2}\right)G_\mathrm{t}(r,\beta,\theta)k(r,\beta,\theta)r\mathrm{d}\beta\mathrm{d}\theta\mathrm{d}r, \tag{34}$$

where $k(r,\beta,\theta)$ is given by (28) for Type I and by (29) for Type II.

Compared to Theorem 1, Corollary 1 calculates the mean interference within the LOS region, which is a disk area of radius R centered at the receiver. As $R\to\infty$, Corollary 1 becomes equivalent to Theorem 1. Physically, this describes a scenario that all links satisfy the LOS condition, which is consistent with the assumption of Theorem 1.

To study the impact of blockages on the mean interference, we extend our result to a probabilistic blockage model. This extension does not affect the G-HCP thinning structure.

Corollary 2. *Under the probabilistic blockage model, the mean interference at the typical receiver can be written as (considering LOS and NLOS)*

$$\begin{aligned}\mathbb{E}^!_{(o,0)}\left[I_{x_o}\right]=&\frac{\lambda_p^2P_0N_\mathrm{t}p_\mathrm{b}}{2\pi\lambda_b}\int_0^{2\pi}\int_0^{2\pi}\int_0^{\infty}\\ &l\left(\sqrt{r^2-2rd\cos\beta+d^2}\right)G_\mathrm{t}(r,\beta,\theta)k(r,\beta,\theta)r\mathrm{d}\beta\mathrm{d}\theta\mathrm{d}r\\ &+\mathbb{E}^!_{(o,0)}\left[I_{x_o,\mathrm{nlos}}\right],\end{aligned} \tag{35}$$

where

$$\mathbb{E}^!_{(o,0)}\left[I_{x_o,\mathrm{nlos}}\right]=\frac{\lambda_p^2P_0N_\mathrm{t}(1-p_\mathrm{b})}{2\pi\lambda_b}\int_0^{2\pi}\int_0^{2\pi}\int_0^{\infty} l_\mathrm{nlos}\left(\sqrt{r^2-2rd\cos\beta+d^2}\right)G_\mathrm{t}(r,\beta,\theta)k(r,\beta,\theta)r\mathrm{d}\beta\mathrm{d}\theta\mathrm{d}r, \tag{36}$$

denotes the mean NLOS interference. $l_\mathrm{nlos}(\cdot)$ is the path-loss function of the NLOS paths.

C. Success Probability

The transmission success probability serves as a fundamental performance metric in wireless network analysis. However, for the hard-core process under consideration, deriving an exact analytical expression for the transmission success probability appears intractable.

To address this issue, we employ ASAPPP to approximate the success probability. This approach is motivated by prior work [20], which derived the success probability $P_\mathrm{PPP}(\theta)$ for a PPP model with nearest transmitter association under the LOS ball assumption.

In this study, we extend the applicability of ASAPPP to Nakagami-M fading, where M is the integer, for the bipolar network. The success probability $P_\phi(\theta)$ for a point process ϕ is approximated via $P_\mathrm{PPP}(\theta)$ adjusted by G

$$P_\phi(\theta)\approx P_\mathrm{PPP}\left(\frac{\theta}{G}\right), \tag{37}$$

where the asymptotic gain G defined in [26] and reflects the relationship between the SIR characteristics of the PPP and ϕ.

We will derive the asymptotic gain G for both Type I and Type II G-HCP under the LOS ball assumption.

Lemma 1. *The asymptotic gain for both Type I and Type II G-HCP with a LOS radius R*

$$G=\mathrm{MISR}_R\frac{2\pi\lambda_b l(d)}{\lambda_p^2P_0N_\mathrm{t}}\left(\int_0^{2\pi}\int_0^{2\pi}\int_0^{\sqrt{R^2-(d\sin\beta)^2}+d\cos\beta} l\left(\sqrt{r^2-2rd\cos\beta+d^2}\right)G_\mathrm{t}(r,\beta,\theta)k(r,\beta,\theta)r\mathrm{d}\beta\mathrm{d}\theta\mathrm{d}r\right)^{-1}, \tag{38}$$

where $k(r,\beta,\theta)$ is given by (28) for Type I and is given by (29) for Type II and MISR_R is the mean interference-to-average-signal ratio of a PPP model with nearest transmitter association and a LOS radius R, written as

$$\begin{aligned}\mathrm{MISR}_R=&\frac{2}{\alpha-2}-\frac{\alpha}{\alpha-2}F_1(\lambda_p\pi R^2)\\ &-\frac{4\lambda_p\pi R^2}{\alpha^2-4}F_2(\lambda_p\pi R^2)+e^{-\lambda_p\pi R^2},\end{aligned} \tag{39}$$

with $F_n(x)$ denoting the confluent hypergeometric function

$$F_n(x)={}_1F_1\left(\frac{\alpha}{2};n+\frac{\alpha}{2};-x\right). \tag{40}$$

Proof. See Appendix A. □

Theorem 2. *The success probability of a receiver in Type I and Type II G-HCP, under LOS conditions with a LOS radius R and independent Nakagami-M fading with integer M, can be approximated as*

$$P_\mathrm{HCP}(\theta)\approx 2\pi\lambda_p\int_0^R e^{-\pi\lambda_p r^2}\|\exp\{\mathbf{C}_M(r)\}\|_1 r\mathrm{d}r,$$

where $\|\cdot\|_1$ represents the sum of the first column and

$$\mathbf{C}_M(r)=\begin{bmatrix}c_0(r)&&&&\\ c_1(r)&c_0(r)&&&\\ c_2(r)&c_1(r)&c_0(r)&&\\ \vdots&&&\ddots&\\ c_{M-1}(r)&\cdots&c_2(r)&c_1(r)&c_0(r)\end{bmatrix},$$

whose exponent is given by (41), where $s=\frac{M\theta r^\alpha}{G}$, $\delta=2/\alpha$, G is defined in Lemma 1 and $E_p(\cdot)$ is the generalized exponential integral.

Proof. See Appendix B. □

To assess the accuracy of the MISR approximation for the Nakagami-M fading, we compare its results with simulation data in this work. Figures 5 and 6 present the success probability under varying values of M and for commonly used values of SIR threshold under the directional RTS/CTS mechanism. The proposed MISR approximation provides accurate approximations for practical success probabilities at low SIR thresholds and the gap between theoretical and simulated results expands with increasing SIR threshold. This observation also clarifies the applicability range of the ASAPPP

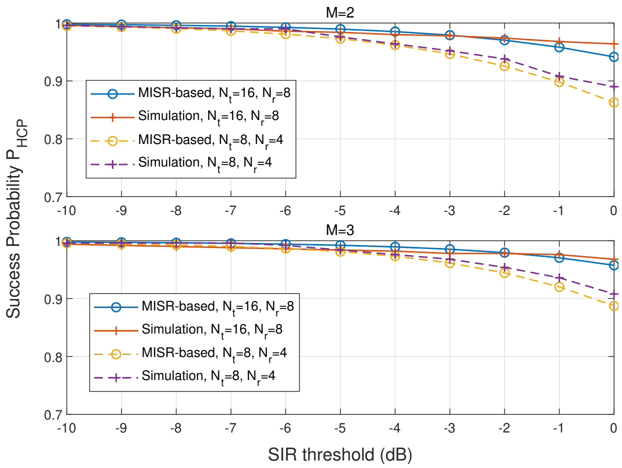

Fig. 5. SIR ccdf for the type I hard-core process and MISR-based approximation for $\lambda_p = 4 \times 10^{-4}\text{m}^{-2}$ and $R = 300$m under the directional RTS/CTS mechanism.

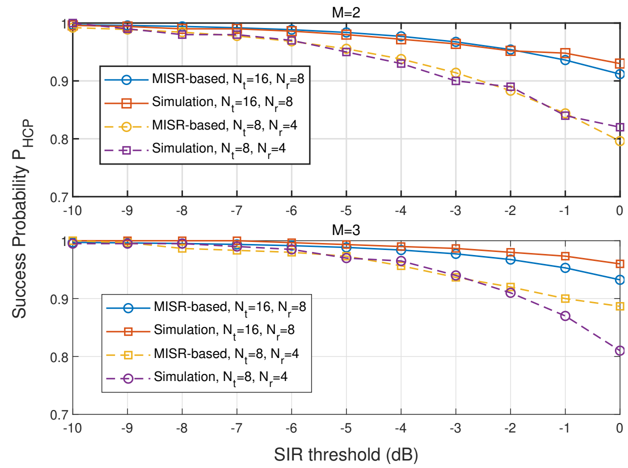

Fig. 6. SIR ccdf for the type II hard-core process and MISR-based approximation for $\lambda_p = 4 \times 10^{-4}\text{m}^{-2}$ and R=300m under the directional RTS/CTS mechanism.

$$c_k(r) = \begin{cases} \pi\lambda_p \left\{ r^2 - R^2 + \delta R^2 \mathbb{E}_g \left[\mathrm{E}_{1+\delta}(sR^{-\alpha}g) \right] - \delta r^2 \mathbb{E}_g \left[\mathrm{E}_{1+\delta}(sr^{-\alpha}g) \right] \right\}, & k = 0, \\ \frac{\pi\delta\lambda_p s^k}{k!} \left\{ R^{2-\alpha k} \mathbb{E}_g \left[g^k \mathrm{E}_{1+\delta-k}(sR^{-\alpha}g) \right] - r^{2-\alpha k} \mathbb{E}_g \left[g^k \mathrm{E}_{1+\delta-k}(sr^{-\alpha}g) \right] \right\}, & k \geq 1. \end{cases} \tag{41}$$

approximation used in this paper. The approximation is mainly reliable at the low SIR threshold regime, which is the operating range emphasized in our numerical evaluation. Therefore, the analytical success probability should be only interpreted as a trend for comparing RTS/CTS mechanisms under a unified framework, rather than an exact prediction.

The success probability for cross-link RTS/CTS is consistently observed to be approximately 1 in simulations and exhibits negligible dependence on the SIR threshold. Due to the directional transmission and the isotropic exclusion region, the asymptotic gain G is greater than 350. This high gain leads to an analytical approximation of 1, which is in excellent agreement with the simulation results. Considering this almost invariant behavior, the results are omitted from Figure 5 and Figure 6.

D. Hidden Nodes

Our preceding analysis demonstrates that the directional RTS/CTS mechanism cannot completely eliminate the hidden terminal problem. We now present a quantitative analysis of this limitation. Specifically, this section develops: an exact mathematical derivation of the expected number of hidden nodes under directional RTS/CTS operation. We focus on the hidden nodes of the typical receiver x_o.

Definition 1. *A* hidden node *y of x_o in the G-HCP is defined as a transmitter that satisfies the following two conditions:*

1) *$y \in \Phi$, i.e., the transmitter is active (retained after the thinning process);*
2) *$x_o \in S_{\text{t}}(y)$, i.e., the typical receiver x_o lies within the exclusion region of transmitter y.*

In other words, a hidden node is an active transmitter whose exclusion region overlaps with the typical receiver, potentially causing interference despite the RTS/CTS mechanism.

The exclusion region of each transceiver pair is caused by the RTS/CTS frame. The other transceiver pairs in the exclusion region of a transceiver pair can decode the RTS/CTS frame transmitted by the transceiver pair. This formal definition captures the essential characteristics of hidden nodes.

Let Φ_{h} be the set of all hidden nodes

$$\Phi_{\text{h}} \triangleq \{y : y \in \Phi \setminus \{o\}, x_o \in S_{\text{t}}(y)\}. \tag{42}$$

The number of hidden nodes N_{h} in the G-HCP is denoted as

$$N_{\text{h}} = \#\Phi_{\text{h}}.$$

Theorem 3. *The expected number of hidden nodes N_{h} in G-HCP is*

$$\mathbb{E}^{!}_{(o,0)}\left[N_{\text{h}}\right] = \frac{\lambda_p^2}{\pi\lambda_b} \int_0^{\pi} \int_0^{R_{\text{t}}\sqrt{1-(\frac{d\sin\beta}{R_{\text{t}}})^2}-d\cos\beta} \int_{-f(r_y)}^{f(r_y)} k\left(r, \beta, \theta + \arcsin\left(\frac{r\cos\beta - d}{r_y}\right)\right) r\mathrm{d}\beta\mathrm{d}r\mathrm{d}\theta, \tag{43}$$

where $k(r, \beta, \theta)$ is given by (28) for Type I and by (29) for Type II, $f(x) = \frac{2\lambda}{\pi N_{\text{t}} d_0} \arccos(\frac{x}{R_{\text{t}}})$ and $r_y = \sqrt{r^2 + d^2 - 2rd\cos\beta}$.

Proof. See Appendix C. □

IV. Implementation of Cross-link RTS/CTS Protocol

A. Channel Access Procedure

Unlike the traditional RTS/CTS mechanism, which operates entirely within a single frequency band, the cross-link RTS/CTS mechanism employs the sub-7 GHz band for control signaling while enabling data transmission over the mm-wave band. This dual-band coordination improves spatial reuse but also requires simultaneous reservation of resources

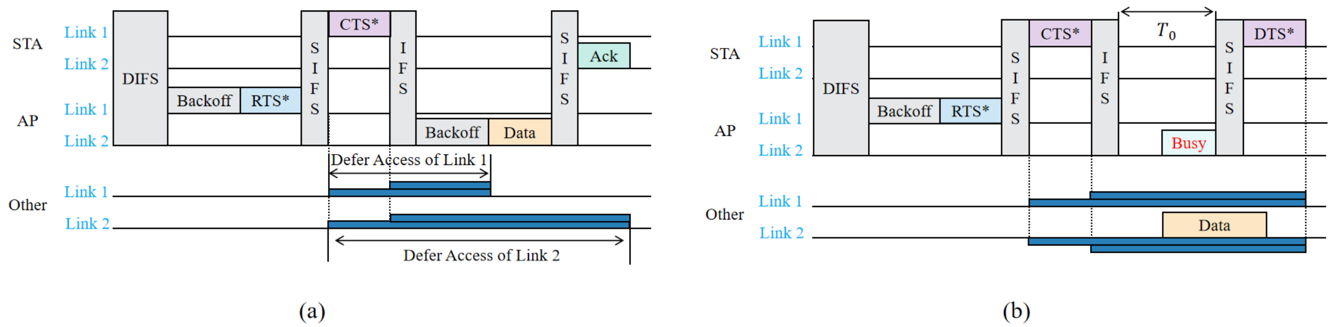

Fig. 7. (a) Message exchange process of the cross-link RTS/CTS mechanism: the AP transmits an RTS* (cross-link RTS frame) over Link 1 (sub-7 GHz); the target STA responds with a CTS* (cross-link CTS frame) on the same link. Neighboring devices then set their NAV timers on Link 1 (sub-7 GHz) according to Duration 1 in the RTS* and CTS* frames, and simultaneously on Link 2 (mm-wave) according to Duration 2. Data transmission subsequently proceeds on the high-rate mm-wave link. (b) Message exchange process in the case where the AP fails to occupy the mm-wave channel within the specified time interval.

in both sub-7 GHz and mm-wave channels, which constitutes the primary challenge of this mechanism.

The overall channel access procedure, illustrated in Fig. 7(a), can be summarized as follows:

- sub-7 GHz channel contention: The AP first contends for access to the sub-7 GHz channel;
- cross-link RTS transmission: Upon successful contention, the AP transmits a cross-link RTS frame over the sub-7 GHz link;
- mm-wave channel assessment: The target STA, after receiving the RTS frame, checks the availability of the mm-wave channel;
- cross-link CTS response: If the mm-wave channel is idle, the STA responds with a cross-link CTS frame on the sub-7 GHz link;
- network reservation: Neighboring devices overhearing either the RTS or CTS frame set their NAV timers for both the sub-7 GHz and mm-wave bands;
- mm-wave data transmission: Following a specified Inter-Frame Space (IFS), the AP proceeds with data transmission on the mm-wave channel.

To reduce the risk of collisions during the transition to mm-wave transmission, a backoff procedure is introduced before the AP occupies the mm-wave channel. However, there is a scenario where the process could not be successfully executed, namely when the mm-wave channel can be acquired.

The cross-link Denial to Send (DTS) frame is designed to handle this scenario. In the case, the frame is used to inform the devices around the STA of releasing NAV reservations, which results from the AP's failure to contend for the mm-wave channel. Due to the uncertainty in mm-wave contention duration, we propose a timeout mechanism: if the STA does not receive any data frame from the AP within a duration T_0 after sending the CTS frame, it broadcasts a cross-link DTS frame, as illustrated in Fig. 7(b). The timeout parameter T_0 is set to the value of $n\times$ slot time, where n denotes the maximum backoff counter. Due to the complexity of the contention for the channel, the likelihood of cross-link DTS occurrences p_{DTS} is difficult to be quantified.

Since the DTS mechanism only releases unnecessary reservations after a failure of the mm-wave channel competition and does not alter the spatial relationship of the active transmitters under the mm-wave network, it is incorporated into the overhead analysis rather than into the G-HCP topology analysis.

B. Implementation Feasibility

In this subsection, we will discuss the implementation feasibility of the cross-link RTS/CTS within the future mm-wave Wi-Fi, named 802.11bq, including required MAC/PHY changes and backward compatibility with legacy devices.

- MAC layer modifications: Modification and resetting of the frame formats for the three corresponding frames are required to support the proposed mechanism. The design of the frames must accommodate the dual-band reservation property of the mechanism. Specifically, each control frame includes two duration fields, enabling neighboring devices to update their NAV timers on both the sub-7 GHz and mm-wave links, as shown in Fig. 8. In addition, the standard Frame Check Sequence (FCS) field, a 32-bit cyclic redundancy check (CRC) located at the end of each Wi-Fi frame, is used for error detection. Definitions of all other fields are summarized in Table I;
- PHY layer modifications: The sub-7GHz PHY layer implementation leverages existing standards. And the mm-wave PHY layer reuses the architectural design of existing sub-7 GHz PHY layer to minimize hardware changes, ensuring low deployment costs;
- backward compatibility: Given the limited large-scale commercial deployment of IEEE 802.11ad/ay devices, backward compatibility with legacy mm-wave Wi-Fi devices is not required for future deployments. Meanwhile, the sub-7 GHz PHY layer adheres to existing standards, ensuring seamless backward compatibility with legacy sub-7 GHz devices (e.g., IEEE 802.11n/ac/ax/be).

C. The Additional Overhead

Compared to the conventional directional RTS/CTS, the cross-link RTS/CTS would introduce the additional overhead without doubt. In the following text, T^a_{RTS}/$T^a_{\mathrm{RTS}*}$, T^a_{CTS}/$T^a_{\mathrm{CTS}*}$ and $T^a_{\mathrm{DTS}*}$ denote the transmission times of

Frame Control	Duration 1	Duration 2	RA	TA	FCS

(a) Cross-link RTS frame format

Frame Control	Duration 1	Duration 2	RA	FCS

(b) Cross-link CTS frame format

Frame Control	Duration 1	Duration 2	RA	NAV-SA	NAV-DA	FCS

(c) Cross-link DTS frame format

Fig. 8. Frame formats of the cross-link RTS/CTS mechanism.

the RTS/cross-link RTS, CTS/cross-link CTS, and cross-link DTS frames, respectively, on channel a. The overhead of conventional directional RTS/CTS is modeled as

$$T_{\mathrm{oh,d}} = \mathbb{E}[T_{\mathrm{bo}}^{\mathrm{mm}}] + T_{\mathrm{RTS}}^{\mathrm{mm}} + T_{\mathrm{SIFS}}^{\mathrm{mm}} + T_{\mathrm{CTS}}^{\mathrm{mm}} \approx 55.3\ \mu s, \quad (44)$$

where $T_{\mathrm{bo}}^{\mathrm{mm}}$ is the mm-wave backoff time, $T_{\mathrm{SITF}}^{\mathrm{mm}}$ is Short Inter-Frame Space (SIFS) of the mm-wave channel. And the approximate value is obtained under the 802.11ad/ay PHY MCS0 assumption, with the minimum bandwidth. For the proposed cross-link RTS/CTS, the overhead is

$$T_{\mathrm{oh,c}} = T_{\mathrm{IFS}}^{\mathrm{mm}} + \mathbb{E}[T_{\mathrm{bo}}^{\mathrm{mm}}] + T_{\mathrm{res}}^{\mathrm{Sub7}}, \quad (45)$$

where $T_{\mathrm{IFS}}^{\mathrm{mm}}$ is IFS before mm-wave data transmission and $T_{\mathrm{res}}^{\mathrm{Sub7}}$ is abstracted as

$$\begin{aligned} T_{\mathrm{res}}^{\mathrm{Sub7}} &= T_{\mathrm{cc}}^{\mathrm{Sub7}} + T_{\mathrm{RTS*}}^{\mathrm{Sub7}} + T_{\mathrm{CTS*}}^{\mathrm{Sub7}} \\ &\quad + T_{\mathrm{DTS*}}^{\mathrm{Sub7}} + 3T_{\mathrm{SIFS}}^{\mathrm{Sub7}} + T_0. \end{aligned} \quad (46)$$

Here, $T_{\mathrm{cc}}^{\mathrm{Sub7}}$ denotes the sub-7 GHz access preparation time before transmitting the cross-link RTS. If the AP has already obtained the sub-7 GHz channel, which may occur when the AP needs to transmit the cross-link RTS frame with priority during an ongoing data transmission, it reduces to a SIFS. Otherwise, it includes the expected sub-7 GHz backoff duration. Therefore, the extra overhead is written as

$$\Delta T = T_{\mathrm{oh,c}} - T_{\mathrm{oh,d}}. \quad (47)$$

Under EHT (802.11be) OFDM with 20 MHz bandwidth, MCS0, a guard interval of 0.8 μs and $n = 31$, ΔT can be approximated as

$$\Delta T \approx \begin{cases} 261.9\ \mu s, \text{if acquired the sub-7 GHz channel} \\ 319.4\ \mu s, \text{others.} \end{cases} \quad (48)$$

Under the proposed cross-link RTS/CTS mechanism, the sub-7 GHz link may remain reserved but carry no payload. To quantify this effect, we define the reserved but idle time on the sub-7 GHz link as

$$\begin{aligned} T_{\mathrm{idle}}^{\mathrm{Sub7}} &= T_{\mathrm{IFS}}^{\mathrm{mm}} + \mathbb{E}[T_{\mathrm{bo}}^{\mathrm{mm}}] + 3T_{\mathrm{SIFS}}^{\mathrm{Sub7}} \\ &\quad + T_0 + (1 - p_{\mathrm{DTS}})T_{\mathrm{DTS*}}^{\mathrm{Sub7}} \\ &\approx 266.3\ \mu s. \end{aligned} \quad (49)$$

Accordingly, the sub-7 GHz reservation inefficiency ratio is defined as

$$\eta_{\mathrm{idle}}^{\mathrm{Sub7}} = \frac{T_{\mathrm{idle}}^{\mathrm{Sub7}}}{T_{\mathrm{oh,c}} - T_{\mathrm{cc}}^{\mathrm{Sub7}}} \approx 0.83. \quad (50)$$

This ratio is used to directly reflect the spectrum utilization inefficiency of sub-7 GHz channel under the cross-link RTS/CTS.

The 802.11ad/ay PHY differs significantly from the sub-7 GHz PHY. Therefore, the aforementioned approximations can only serve as a reference and cannot fully reflect the additional overhead introduced by cross-link RTS/CTS in future mm-wave Wi-Fi. The timeout parameter T_0 is one of the most important factors in the overhead evaluation. In particular, if T_0 is too small, an ongoing backoff process may be mistakenly treated as a failure to obtain channel access, whereas an excessively large T_0 unnecessarily increases the reservation overhead.

For each overhearing device, the NAV maintenance cost increases from one timer state in conventional single-band RTS/CTS to two timer states in the proposed dual-band reservation. When an overhearing device receives a cross-link control frame, it needs to perform two NAV maintenance operations $C_{\mathrm{NAV}}^{\mathrm{cross}} = 2$, namely, one for the sub-7 GHz band and the other for the mm-wave band, whereas only one NAV maintenance operation $C_{\mathrm{NAV}}^{\mathrm{conv}} = 1$ is required in conventional single-band RTS/CTS.

D. Hybrid RTS/CTS Selection

Motivated by the difference between the two RTS/CTS mechanisms, we propose a hybrid switching rule. This hybrid policy provides an actionable design rule: short transmission opportunities (TXOPs) should use the conventional directional RTS/CTS to avoid excessive signaling overhead, while long transmissions should switch to cross-link RTS/CTS to avoid collisions.

$$\text{Mode} = \begin{cases} \text{cross-link RTS/CTS}, & T_{\mathrm{TXOP}} > T_{\mathrm{th}}, \\ \text{directional RTS/CTS}, & \text{otherwise}, \end{cases} \quad (51)$$

where T_{TXOP} denotes the TXOP duration, representing the required channel occupation time, and T_{th} is the pre-defined threshold for mode switching.

Fig. 9 presents the system-level simulation results. In this simulation, we adopt a silencing strategy that better reflects practical systems, in which only active transmitters can silence surrounding devices. The number of propagation time slots,

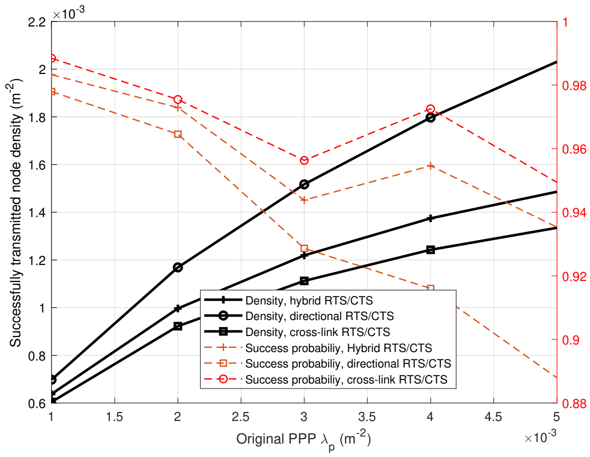

Fig. 9. The system-level simulation of the three RTS/CTS mechanisms.

denoted by T_{TXOP}, required by each transmitter follows the distribution

$$p = \begin{cases} 0.2, & T_{\mathrm{TXOP}} = 0, \\ 0.2, & T_{\mathrm{TXOP}} = 1, \\ 0.4, & T_{\mathrm{TXOP}} = 2, \\ 0.2, & T_{\mathrm{TXOP}} = 3, \end{cases} \tag{52}$$

Moreover, T_{th} is set as 3. As shown in Fig. 9, where the fixed threshold is intended to demonstrate the feasibility of the hybrid RTS/CTS. The hybrid RTS/CTS lies between the other two mechanisms, providing a compromise between reliability and throughput.

In fact, T_{th} is mainly determined by the active node density, since the density directly affects the probability of hidden node. When the active node density is low, the hidden terminal problem is relatively weak. In this case, the threshold should be relatively large, so that cross-link RTS/CTS is activated only for long TXOPs to reduce the overhead. As the active node density increases, the probability of the collisions under directional RTS/CTS becomes higher. Therefore, the threshold should decrease with the active node density, allowing cross-link RTS/CTS to be used for a wider range of TXOP durations to achieve a high reliability.

However, the active node density is difficult to measure in practice. Therefore, measurable interference-related indicators can be used to adjust the threshold dynamically in practical deployment, as the interference level reflects the active node density to a certain extent.

V. Performance Comparison Under a Unified Benchmark

A. Unified Benchmark

To ensure a fair and consistent comparison between the proposed cross-link RTS/CTS mechanism and the conventional directional RTS/CTS mechanism, it is essential to establish a unified performance benchmark. A key consideration in this comparison is whether to normalize the exclusion region size across different configurations.

Assuming omnidirectional reception, the receive antenna gain is set to unity. A receiver can successfully decode a frame in either the sub-7 GHz or mm-wave band when the received power satisfies

$$P_{\mathrm{rx}} \geq P_{\mathrm{rx(th)}}, \tag{53}$$

where $P_{\mathrm{rx(th)}}$ denotes the minimum detectable power threshold for the corresponding frequency band.

The maximum transmission ranges R_1 for frequency band 1 and R_2 for frequency band 2, respectively, under the Friis model are related by

$$\frac{R_1}{R_2} = \sqrt{\frac{P_1}{P_2} \cdot \frac{G_1}{G_2} \cdot \frac{f_2}{f_1}}, \tag{54}$$

where P_i, G_i and f_i are the transmission power of the single antenna, the transmitting antenna gain and frequency of frequency band i, respectively. For the mm-wave band, the directional antenna gain in the main-lobe direction equals the number of antenna elements, while for the sub-7 GHz band, the omnidirectional transmit gain is unity.

In this study, the exclusion region size corresponding to the cross-link RTS/CTS mechanism with a transmit power of 20 mW is adopted as the reference. The exclusion regions for both the directional and cross-link RTS/CTS mechanisms under other transmit powers are then scaled according to (54).

B. Performance Comparison

In this section, the terms *cRTS/CTS* and *dRTS/CTS* refer to the cross-link RTS/CTS and directional RTS/CTS mechanisms, respectively. For the reference configuration, the receiver range is set to $R_{\mathrm{r}} = 4d$ and the transmitter range to $R_{\mathrm{t}} = 4.8d$ for the cRTS/CTS scheme operating with a transmission power of 20 mW. The default system parameters are summarized in Table II. The transmission power per mm-wave antenna is $P_0 = 20$ mW, and the path loss follows $l(r) = (1 + r^{\alpha})^{-1}$. The loss exponent of LOS paths, denoted by α, is given in Table II, and that of NLOS paths is 3.

In the following figures, the legend labels "Type I" and "Type II" correspond to the Type I and Type II G-HCPs, respectively. The label $P_{\text{sub-7}}$ denotes the sub-7 GHz transmission power for cRTS/CTS. Two configurations of cRTS/CTS are evaluated, with $P_{\text{sub-7}} = 20$ mW and $P_{\text{sub-7}} = 40$ mW, respectively.

Figure 10 illustrates the relationship between the active node density λ_b and the original PPP intensity λ_p under various RTS/CTS configurations. For all Type I models, the active node density λ_b first increases with λ_p and then decreases after reaching a peak. The maximum occurs when $\lambda_p = \frac{1}{V_o}$, where V_o denotes the area of the exclusion region, yielding a peak value of $\frac{1}{V_o} e^{-1}$. In contrast, for Type II models, λ_b increases monotonically with λ_p and asymptotically approaches the reciprocal of the exclusion region. It can also be observed that the dRTS/CTS mechanism yields a higher λ_b than cRTS/CTS under identical exclusion conditions, indicating that cRTS/CTS achieves a stronger suppression of concurrent transmissions and thus a more effective interference mitigation.

Figure 11 depicts the variation of the mean interference with respect to the original PPP intensity λ_p. For all Type I

TABLE I
CROSS-LINK CONTROL FRAME FIELD DEFINITIONS

Frame Type	Duration 1 / Duration 2	RA Field	Additional Fields
cross-link RTS	the time that the entire transmission session occupies the sub-7 GHz / mm-wave channels	MAC address of the recipient STA	**TA:** MAC address of the transmitting STA
cross-link CTS	Remaining time on sub-7 GHz / mm-wave channels	TA from the cross-link RTS frame	–
cross-link DTS	Remaining time on sub-7 GHz / mm-wave channels	TA from the cross-link RTS frame	**NAV-SA/NAV-DA:** MAC addresses of the STAs transmitting the cross-link RTS / cross-link CTS

TABLE II
SYSTEM PARAMETERS

Symbol	Parameter	Value
R	LOS radius	300 m
d	Transmitter–receiver distance	20 m
N_{t}	Number of transmit antenna elements	16
N_{r}	Number of receive antenna elements	8
θ	SIR threshold	-5 dB
α	Path loss exponent	2.1

models, the mean interference first increases with λ_p and then decreases after reaching a peak. Similar to Type I models, the trend is observed for Type II models, where the mean interference evolves consistently with the active node density. In particular, the mean interference in Type II models increases monotonically with λ_p and gradually converges to a constant value. It is also observed that dRTS/CTS exhibits higher mean interference than cRTS/CTS under both Type I and Type II configurations, even though its active node density is lower. This seemingly counterintuitive behavior stems from the inherent differences in the exclusion regions of the two RTS/CTS mechanisms and the directional gain of antenna arrays. When $\lambda_p \to 0$, both mechanisms can be approximated as PPPs with identical intensities, since the exclusion effect becomes negligible. The only distinction lies in the spatial distribution of transmitters: nodes under dRTS/CTS can be located closer to the typical receiver, leading to stronger interference. Overall, cRTS/CTS provides a clear advantage by maintaining a lower interference level for most density regimes, thereby achieving superior link quality and more stable network performance.

Figure 12 presents the variation of the mean interference under the probabilistic blockage model introduced in Corollary 2 with respect to the original PPP intensity. Compared with the results of the LOS ball model in Figure 11, the overall qualitative trends remain unchanged: cRTS/CTS still achieves lower mean interference than dRTS/CTS under both Type I and Type II thinning for most density regimes, which is consistent with Figure 11. These results indicate that the main conclusion of Figure 11 is unaffected by the blockage modeling assumption.

Figure 13 illustrates the variation of a key performance metric, the product of the success probability and the active transmitter density λ_b. This metric effectively represents the network throughput. For Type I schemes, the throughput trends

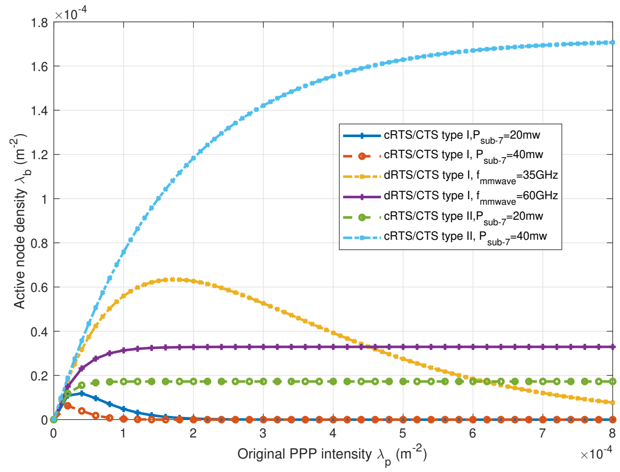

Fig. 10. Active node density λ_b as a function of the original PPP intensity λ_p for various RTS/CTS configurations.

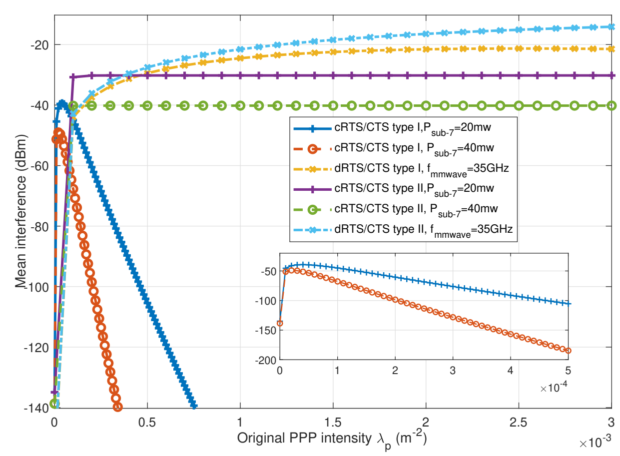

Fig. 11. Mean interference as a function of the original PPP intensity λ_p under different RTS/CTS mechanisms

closely follow those of the mean interference. Both cRTS/CTS and dRTS/CTS exhibit an initial increase in throughput as λ_p rises, followed by a decline beyond a certain point, indicating the existence of an optimal network density for Type I configurations. A distinct behavior is observed under Type II schemes. For cRTS/CTS, the throughput monotonically follows the variation of mean interference, while for dRTS/CTS, a non-monotonic pattern emerges—throughput first increases,

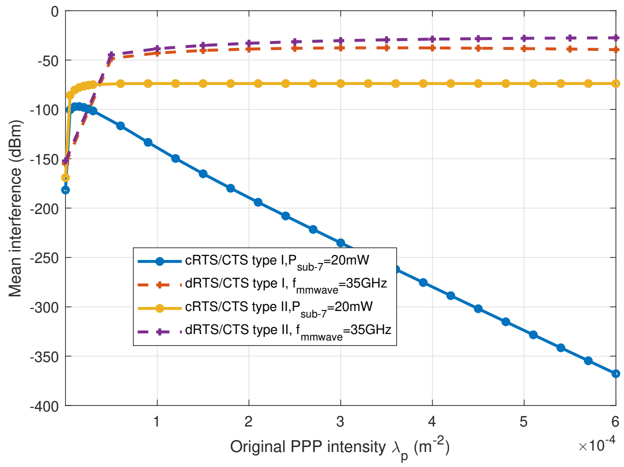

Fig. 12. Mean interference introduced in Corollary 2 as a function of the original PPP intensity λ_p for various RTS/CTS configurations.

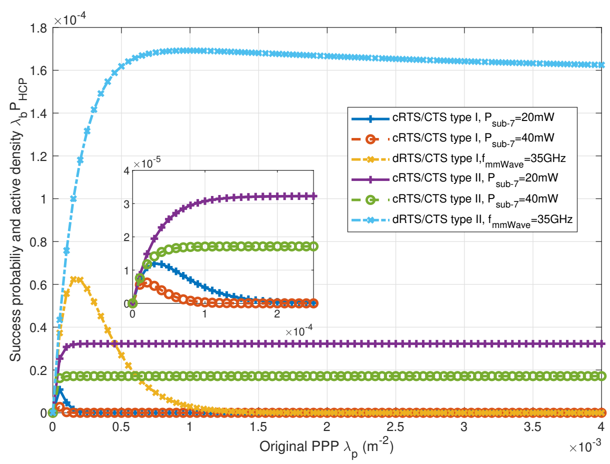

Fig. 13. The network throughput as as a function of the original PPP intensity λ_p. This metric is defined as the product of the success probability and the active transmitter density and provides a measure of network throughput.

then slightly decreases, and finally converges to a constant level. This divergence can be explained by the interference characteristics shown in Figure 11. At low λ_p, throughput for both mechanisms is mainly governed by the active node density. However, when $\lambda_p > 1 \times 10^{-3}\mathrm{m}^{-2}$, the continuously increasing interference in dRTS/CTS leads to a reduction in success probability that outweighs the gain from higher node density, resulting in the observed throughput trend. Overall, despite the higher interference levels, dRTS/CTS achieves superior throughput performance compared to cRTS/CTS, benefiting from its more efficient spatial reuse of the wireless medium.

Figure 14 illustrates the relationship between the mean number of hidden nodes in Type I dRTS/CTS and the original PPP intensity λ_p under different system configurations. For Type I models, the mean number of hidden nodes first increases with λ_p and then decreases after reaching a peak, indicating the existence of an optimal intensity that maximizes hidden nodes occurrence. A comparison between the second curve (35 GHz, $N_\mathrm{r} = 16$, $N_\mathrm{r} = 8$, $d = 20$ m) and the fifth curve

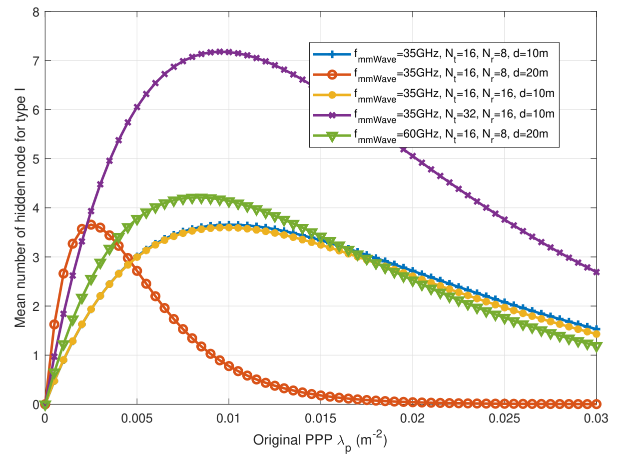

Fig. 14. The mean number of hidden nodes for Type I under different system configurations

(60 GHz, $N_\mathrm{r} = 16$, $N_\mathrm{r} = 8$, $d = 20$ m) shows that higher carrier frequency results in a larger maximum mean number of hidden nodes. For a fixed frequency (35 GHz) and link distance ($d = 10$ m), increasing N_r significantly raises the peak value, whereas increasing N_r yields only a marginal impact. This observation indicates that the hidden-node count is mainly influenced by the transmitter-side exclusion region, since a larger N_r allows more distant transmitters to become hidden nodes despite the narrower beam coverage. Comparing the first (35 GHz, $N_\mathrm{r} = 16$, $N_\mathrm{r} = 8$, $d = 10$ m) and second (35 GHz, $N_\mathrm{r} = 16$, $N_\mathrm{r} = 8$, $d = 20$ m) curves reveals that both achieve similar maximum values but at different λ_p, implying that merely scaling the exclusion region size, without altering its spatial structure, is insufficient to mitigate the hidden-node issue. Overall, all curves exhibit peak values exceeding 3.5, highlighting the severity of the hidden-node problem in Type I dRTS/CTS within a moderate density range. As λ_p continues to increase, the mean number of hidden nodes gradually converges to zero, suggesting that the likelihood of hidden-node occurrence diminishes in denser Type I networks.

Figure 15 illustrates the relationship between the mean number of hidden nodes in Type II dRTS/CTS and the original PPP intensity λ_p under different system configurations. For Type II models, the mean number of hidden nodes increases monotonically with λ_p and gradually converges to a steady-state value as λ_p grows large. This steady value exhibits similar parameter-dependent behavior to the peak value observed in the Type I case. The fundamental distinction between Type I and Type II lies in their asymptotic behavior: in Type I, increasing node density eventually suppresses hidden-node occurrences, whereas in Type II, the problem persists even at high densities. Furthermore, both the steady value for Type II and the peak value for Type I are consistently higher in dRTS/CTS than in cRTS/CTS, indicating a more severe hidden-node issue and consequently lower link reliability in directional RTS/CTS networks.

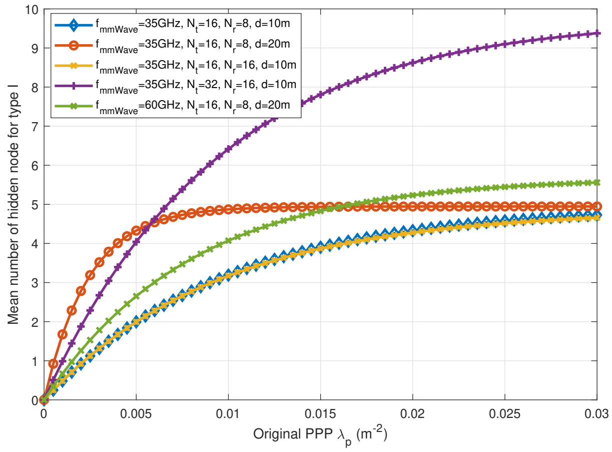

Fig. 15. The mean number of hidden nodes for Type II under different system configurations

VI. Conclusion

This paper presented a marked point process framework to characterize the spatial configuration of transceivers operating under the RTS/CTS handshake mechanism in WLANs. The proposed model accommodates both omnidirectional and directional communication scenarios, enabling a unified analysis of interference and throughput performance.

Numerical results demonstrate distinct performance trends between the cross-link RTS/CTS and the directional RTS/CTS schemes. The cross-link RTS/CTS ensures more reliable link quality by effectively mitigating interference, but at the cost of reduced overall throughput. In contrast, the directional RTS/CTS achieves higher network throughput, yet suffers from degraded link reliability and a pronounced hidden node problem. These findings reveal a fundamental design trade-off between link reliability and spatial reuse. The appropriate choice between the two protocols should thus depend on the network's target performance objectives—whether prioritizing throughput efficiency or communication robustness.

Appendix A
Proof of Lemma 1

The asymptotic gain G is defined as

$$G = \frac{\mathrm{MISR}_R}{\mathrm{MISR}_{\mathrm{G-HCP}}}, \tag{55}$$

where $\mathrm{MISR}_{\mathrm{G-HCP}}$ is the mean interference-to-average-signal ratio of the G-HCP model, denoted as

$$\mathrm{MISR}_{\mathrm{G-HCP}} = \frac{\mathbb{E}^{!}_{(o,0)}[I_{x_o,R}]}{l(d)}. \tag{56}$$

Next, we focus on MISR_R, which is the mean interference-to-average-signal ratio of the PPP model with nearest transmitter association and a LOS radium R. Letting R_k be the distance from the typical user to the k-th nearest cellular BS, $v_k = R_1/R_k$ is the distance ratio. The interference-to-average-signal ratio for the LOS region, denoted by $\bar{\mathrm{ISR}}_R$, is defined as

$$\bar{\mathrm{ISR}}_R = \sum_{i=2}^{\infty} v_i^{\alpha} \mathbb{P}(N \geq i), \tag{57}$$

where $\mathbb{P}(N \geq i)$ denotes the probability that the number of nodes is no less than i within the LOS region. For a PPP where the mean number of nodes in the LOS region is $N_{\mathrm{LR}} = \lambda_p \pi R^2$, $\mathbb{P}(N \geq i)$ follows as

$$\mathbb{P}(N \geq i) = \sum_{k=i}^{\infty} \frac{N_{\mathrm{LR}}^k e^{-N_{\mathrm{LR}}}}{i!}. \tag{58}$$

Therefore, $\mathrm{MISR}(R)$ can be written as

$$\begin{aligned}\mathrm{MISR}_R &\triangleq \mathbb{E}[\bar{\mathrm{ISR}}_R] \\ &= e^{-N_{\mathrm{LR}}} \sum_{i=2}^{\infty} \frac{\Gamma(1+\frac{\alpha}{2})\Gamma(i)}{\Gamma(i+\frac{\alpha}{2})} \sum_{k=i}^{\infty} \frac{N_{\mathrm{LR}}^k}{k!},\end{aligned} \tag{59}$$

and MISR_{∞} follows as [26]

$$\mathrm{MISR}_{\infty} \triangleq \mathbb{E}(\bar{\mathrm{ISR}}_{\infty}) = \frac{2}{\alpha-2}.$$

Since the direct evaluation of (59) is computationally challenging, we introduce $g(R)$ defined as:

$$\begin{aligned}g(R) &= \mathrm{MISR}_{\infty} - \mathrm{MISR}_R \\ &= e^{-N_{\mathrm{LR}}} \sum_{i=1}^{\infty} \frac{i!}{(1+\frac{\alpha}{2})_i} \sum_{k=0}^{i} \frac{N_{\mathrm{LR}}^k}{k!},\end{aligned} \tag{60}$$

where $(x)_i = \frac{\Gamma(x+i)}{\Gamma(x)}$ is the Pochhammer symbol. Changing the order of summation, (60) can be rewritten as

$$\begin{aligned}g(R) &= e^{-N_{\mathrm{LR}}} \left(\sum_{k=0}^{\infty} \frac{N_{\mathrm{LR}}^k}{k!} \sum_{i=k}^{\infty} \frac{i!}{(1+\frac{\alpha}{2})_i} - 1 \right) \\ &= e^{-N_{\mathrm{LR}}} \left(\sum_{k=0}^{\infty} \frac{N_{\mathrm{LR}}^k}{(1+\frac{\alpha}{2})_k} \sum_{i=0}^{\infty} \frac{(k+1)_i}{(k+1+\frac{\alpha}{2})_i} - 1 \right) \\ &\overset{(b)}{=} e^{-N_{\mathrm{LR}}} \left(\sum_{k=0}^{\infty} \frac{N_{\mathrm{LR}}^k (2k+\alpha)}{(1+\frac{\alpha}{2})_k (\alpha-2)} - 1 \right) \\ &\overset{(c)}{=} \frac{\alpha}{\alpha-2} F_1(N_{\mathrm{LR}}) + \frac{4N_{\mathrm{LR}}}{\alpha^2-4} F_2(N_{\mathrm{LR}}) - e^{-N_{\mathrm{LR}}}.\end{aligned} \tag{61}$$

where step (b) follows from the Gauss's Hypergeometric Theorem and (c) follows from the Kummer's transformation for the confluent hypergeometric function with $F_n(x)$ denoting

$$F_n(x) = {}_1F_1\left(\frac{\alpha}{2}; n+\frac{\alpha}{2}; -x\right). \tag{62}$$

Therefore, MISR_R can be written as

$$\mathrm{MISR}_R = \frac{2}{\alpha-2} - g(R),$$

which can be substituted into (55) to get the equation in Lemma 1.

Appendix B
Proof of Theorem 2

The cumulative distribution (cdf) of the SIR is

$$F_{\mathrm{SIR}}(\theta) = \mathbb{P}(h < \theta \bar{\mathrm{ISR}}), \tag{63}$$

where h follows a gamma distribution Gamma$(M, \frac{1}{M})$.

Considering that $M \in \mathbb{N}$ and $x \to 0$, the cdf of h is

$$F_h(x) = 1 - \sum_{k=0}^{M-1} \frac{(Mx)^k e^{-Mx}}{k!} \sim \frac{M^{M-1}}{\Gamma(M)} x^M. \tag{64}$$

Thus, we have

$$\mathbb{P}(h < \theta \bar{\mathrm{ISR}} \mid \bar{\mathrm{ISR}}) = F_h(\theta \bar{\mathrm{ISR}}) \sim \frac{M^{M-1}}{\Gamma(M)} \theta^M \cdot \bar{\mathrm{ISR}}^M. \tag{65}$$

Taking the expectation, we obtain

$$\mathbb{P}(\mathrm{SIR} < \theta) \sim \frac{M^{M-1}}{\Gamma(M)} \theta^M \cdot \mathbb{E}(\bar{\mathrm{ISR}}^M). \tag{66}$$

Based on the traditional ASAPPP, the approximation of $\mathbb{P}(h > \theta \bar{\mathrm{ISR}})$ is written as

$$\mathbb{P}(h > \theta \bar{\mathrm{ISR}}) \approx \mathbb{P}_{\mathrm{PPP}}(h > \theta / G_M), \tag{67}$$

where

$$G_M = \left(\frac{\mathbb{E}(\bar{\mathrm{ISR}}^M)}{\mathbb{E}(\bar{\mathrm{ISR}}^M_{\mathrm{G-HCP}})} \right)^{\frac{1}{M}}. \tag{68}$$

The approximation of G_M is given by [26]

$$G_M \approx G, \tag{69}$$

where G is given by Lemma 1.

Under Nakagami-M fading conditions, the success probability $\mathbb{P}_{\mathrm{PPP}}(\mathrm{SIR} > \theta)$ in the cellular network for a given SIR threshold θ is given in [20]. Substituting (69) into (67), Theorem 2 has been proved.

Appendix C
Proof of Theorem 3

First, we present the reduced second-order factorial measure $\mathcal{K}_{(r,\beta,\theta)}(B \times L)$ for the marked point process, under the assumption that the transmitter corresponding to (r, β, θ) is contained within the point process Φ. And $\lambda_b \mathcal{K}_{(r,\beta,\theta)}(B \times L)$ is the expected number of points located in B with marks taking values in L under the condition of the potential transmitter $y = (r, \beta) \in \Phi$.

Based on $\mathcal{K}_{(r,\beta,\theta)}(B \times L), B \subset \mathbb{R}^2, L \subset [0, 2\pi]$, the expectation of hidden nodes $\mathbb{E}^!_{(o,0)}[N]$ can be written as

$$\mathbb{E}^!_{(o,0)}[N_{\mathrm{h}}] = \mathbb{E}^!_{(o,0)} \left(\sum_{(y,\theta) \in \tilde{\Phi}} \mathbb{1}(x_o \in S_y) \right) = \lambda_b \int_{\mathbb{R}^2 \times [0,2\pi]} \mathbb{1}(x_o \in S_{\mathrm{t}}(y)) \mathcal{K}_{(o,0)}(\mathrm{d}(y, \theta)). \tag{70}$$

The second-order factorial moment measure for the marked point process can be formally expressed as

$$\begin{aligned} &\alpha^{(2)}(B_1 \times B_2 \times L_1 \times L_2) \\ &= \mathbb{E} \left(\sum_{y_1, y_2 \in \Phi}^{\neq} 1_{B_1}(y_1) 1_{B_2}(y_2) 1_{L_1}(\theta_1) 1_{L_2}(\theta_2) \right) \\ &= \mathbb{E}_{y_1 \in \Phi} \left(\mathbb{E} \left(\sum_{y_2 \in \Phi}^{y_2 \neq y_1} 1_{B_2}(y_2) 1_{L_2}(\theta_2) \right) \right) \\ &\overset{(a)}{=} \frac{\lambda_b^2}{2\pi} \int_{B_1 \times L_1} \mathcal{K}_{(y,\theta)}((B_2 - y) \times L_2) \mathrm{d}(y, \theta) \\ &\overset{(b)}{=} \int_{B_1 \times L_1} \left(\int_{(B_2 - y_1) \times L_2} \varrho^{(2)}(y_2, \theta_1, \theta_2) \mathrm{d}(y_2, \theta_2) \right) \mathrm{d}(y_1, \theta_1), \end{aligned} \tag{71}$$

where (a) follows that $\mathbb{E}\left(\sum_{y_2 \in \Phi}^{y_2 \neq y_1} 1_{B_2}(y_2) 1_{L_2}(\theta_2)\right)$ is the expected number of points located in B_2 with marks taking values in L_2 under $y_1 \in \Phi$, i.e., $\lambda_b \mathcal{K}_{(y_1,\theta)}((B_2 - y_1) \times L_2)$ and (b) follows the definition of $\alpha^{(2)}$ and the second-order product $\varrho^{(2)}$.

The second-order product density $\varrho^{(2)}$ and $\mathcal{K}_{(o,0)}(B \times L)$ satisfy:

$$\mathcal{K}_{(o,0)}(d(y, \theta)) = \frac{2\pi}{\lambda_b^2} \varrho^{(2)}(y, 0, \theta) \mathrm{d}(y, \theta), \tag{72}$$

where $\mathrm{d}(y, \theta)$ denotes the differential measure in polar coordinates. Therefore, $\mathbb{E}^!_{(o,0)}[N_{\mathrm{h}}]$ can be written as

$$\mathbb{E}^!_{(o,0)}[N_{\mathrm{h}}] = \frac{2\pi}{\lambda_b} \int_{\mathbb{R}^2 \times [0,2\pi]} \mathbb{1}(x_o \in S_{\mathrm{t}}(y)) \varrho^{(2)}(y, 0, \theta) \mathrm{d}(y, \theta). \tag{73}$$

$\varrho^{(2)}(y, \theta_0, \theta)$ admits the explicit form

$$\varrho^{(2)}(y, \theta_0, \theta) = \frac{\lambda_p^2}{4\pi^2} k(y, \theta_0, \theta), \tag{74}$$

where $k(y, \theta_0, \theta)$ represents the probability that two transceiver pairs (o, θ_0) and (y, θ) are both within $\tilde{\Phi}$.

Obviously, under the condition that one transceiver pair is the typical pair, $k(y, \theta_0, \theta)$ can be written as:

$$k(y, \theta_0, \theta) = k(r, \beta, \theta), \tag{75}$$

where (r, β, θ) is the parameter of the other transceiver pair.

Substituting (74) into (73), we get

$$\mathbb{E}^!_{(o,0)}[N_{\mathrm{h}}] = \frac{\lambda_p^2}{2\pi\lambda_b} \int_0^\infty \int_0^{2\pi} \int_0^{2\pi} \mathbb{1}(x_o \in S_{\mathrm{t}}(y)) k(r, \beta, \theta) r \mathrm{d}r \mathrm{d}\beta \mathrm{d}\theta, \tag{76}$$

where $S_{\mathrm{t}}(y)$ is the transmitter's exclusion region of the transceiver pair (r, β, θ).

The key point is to derive $\mathbb{1}(x_o \in S_{\mathrm{t}}(y))$. y is the transmitter of the transceiver (r, β, θ). Assuming that r_y is the distance of x_o and y and θ_y is the angle difference between the vector $\overrightarrow{yx_o}$ and $\overrightarrow{v} = (\cos(\theta), \sin(\theta))$, if $x_o \in S_{\mathrm{t}}(y)$, r_y and θ_y satisfy:

$$|\theta_y| \le \frac{2\lambda}{\pi N_{\mathrm{t}} d_0} \arccos(\frac{r_y}{R_{\mathrm{t}}}). \tag{77}$$

Substituting (77) into (76), (76) can be written as:

$$\mathbb{E}^{!}_{(o,0)}\left[N_{\mathrm{h}}\right] = \frac{\lambda_p^2}{\pi\lambda_b}\int_0^{\pi}\int_0^{\infty}\int_{-\frac{2\lambda}{\pi N_{\mathrm{t}} d_0}\arccos(\frac{r_y}{R_{\mathrm{t}}})}^{\frac{2\lambda}{\pi N_{\mathrm{t}} d_0}\arccos(\frac{r_y}{R_{\mathrm{t}}})} k\left(r,\beta,\theta-\arccos\left(\frac{r\cos\beta-d}{r_y}\right)\right) r\mathrm{d}\beta\mathrm{d}r\mathrm{d}\theta, \tag{78}$$

where $r_y = \sqrt{r^2+d^2-2rd\cos\beta}$.

Noting $r_y \leq R_{\mathrm{t}}$, r should satisfy:

$$r \leq R_{\mathrm{t}}\sqrt{1-(\frac{d\sin\beta}{R_{\mathrm{t}}})^2} - d\cos\beta, \tag{79}$$

which follows the equation:

$$r^2+d^2-r_y^2 = 2rd\cos\beta. \tag{80}$$

Substituting (79) into (78) has been mentioned above completes the proof of Theorem 3.

References

[1] Z. Chen, Y. Zhong, and H. H. Yang, "Interference in Millimeter-Wave Systems with Directional RTS/CTS Handshake," in *23rd International Symposium on Modeling and Optimization in Mobile, Ad Hoc, and Wireless Networks (WiOpt)*, 2025, pp. 1–7.

[2] B. Crow, I. Widjaja, J. Kim, and P. Sakai, "IEEE 802.11 Wireless Local Area Networks," *IEEE Communications Magazine*, vol. 35, no. 9, pp. 116–126, 1997.

[3] "IEEE Standard for Telecommunications and Information Exchange Between Systems - LAN/MAN Specific Requirements - Part 11: Wireless Medium Access Control (MAC) and Physical Layer (PHY) Specifications: High Speed Physical Layer in the 5 GHz band," *IEEE Std 802.11a-1999*, pp. 1–102, 1999.

[4] S. Lindroos, A. Hakkala, and S. Virtanen, "Battle of the Bands: A Long-Term Analysis of Frequency Band and Channel Distribution Development in WLANs," *IEEE Access*, vol. 10, pp. 61 463–61 471, 2022.

[5] G. Naik, J.-M. Park, J. Ashdown, and W. Lehr, "Next Generation Wi-Fi and 5G NR-U in the 6 GHz Bands: Opportunities and Challenges," *IEEE Access*, vol. 8, pp. 153 027–153 056, 2020.

[6] P. Zhou, K. Cheng, X. Han, X. Fang, Y. Fang, R. He, Y. Long, and Y. Liu, "Ieee 802.11ay-based mmwave wlans: Design challenges and solutions," *IEEE Communications Surveys & Tutorials*, vol. 20, no. 3, pp. 1654–1681, 2018.

[7] Ericsson, "Ericsson Mobility Report November 2023," Tech. Rep. [Online]. Available: https://www.ericsson.com/en/reports-and-papers/mobility-report/key-figures

[8] F. Tobagi and L. Kleinrock, "Packet Switching in Radio Channels: Part II - The Hidden Terminal Problem in Carrier Sense Multiple-Access and the Busy-Tone Solution," *IEEE Transactions on Communications*, vol. 23, no. 12, pp. 1417–1433, 1975.

[9] S. Misra, "Millimeter Wave Wireless Communications (Rappaport, T., et al; 2014) [Book review]," *IEEE Wireless Communications*, vol. 22, no. 5, pp. 6–7, 2015.

[10] "IEEE Draft Standard for Information technology–Telecommunications and information exchange between systems Local and metropolitan area networks–Specific requirements - Part 11: Wireless LAN Medium Access Control (MAC) and Physical Layer (PHY) Specifications Amendment: Enhancements for Extremely High Throughput (EHT)," *IEEE P802.11be/D3.0, January 2023*, pp. 1–999, 2023.

[11] C. Chen, X. Chen, D. Das, D. Akhmetov, and C. Cordeiro, "Overview and Performance Evaluation of Wi-Fi 7," *IEEE Communications Standards Magazine*, vol. 6, no. 2, pp. 12–18, 2022.

[12] S. Lian, J. Tong, and L. Fu, "Dynamic Channel Allocation via Bandit Learning for WiFi 7 Networks with Multi-Link Operation," in *2025 IEEE Wireless Communications and Networking Conference (WCNC)*, 2025, pp. 1–6.

[13] IEEE 802.11 Working Group, "IMMW System Reuses," PowerPoint presentation, Mar. 2024, iEEE 802.11 Working Group Document 11-25-0238-00-00BQ. [Online]. Available: https://mentor.ieee.org/802.11/dcn/25/11-25-0238-00-00bq-immw-system-reuses.pptx

[14] IEEE P802.11 Wireless LANs, "802.11 IMMW Proposed PAR," IEEE, Standard 802.11-24/0116r7, Jan 2024, revision 7. [Online]. Available: https://mentor.ieee.org/802.11/dcn/24/11-24-0116-07-immw-immw-draft-proposed-par.docx

[15] T. Bai and R. W. Heath, "Coverage and Rate Analysis for Millimeter-Wave Cellular Networks," *IEEE Transactions on Wireless Communications*, vol. 14, no. 2, pp. 1100–1114, 2015.

[16] S. M. Azimi-Abarghouyi, B. Makki, M. Nasiri-Kenari, and T. Svensson, "Stochastic Geometry Modeling and Analysis of Finite Millimeter Wave Wireless Networks," *IEEE Transactions on Vehicular Technology*, vol. 68, no. 2, pp. 1378–1393, 2019.

[17] H. Wei, N. Deng, and M. Haenggi, "Performance Analysis of Inter-Cell Interference Coordination in mm-Wave Cellular Networks," *IEEE Transactions on Wireless Communications*, vol. 21, no. 2, pp. 726–738, 2022.

[18] M. R. Akdeniz, Y. Liu, M. K. Samimi, S. Sun, S. Rangan, T. S. Rappaport, and E. Erkip, "Millimeter Wave Channel Modeling and Cellular Capacity Evaluation," *IEEE Journal on Selected Areas in Communications*, vol. 32, no. 6, pp. 1164–1179, 2014.

[19] T. Bai and R. W. Heath, "Coverage analysis for millimeter wave cellular networks with blockage effects," in *2013 IEEE Global Conference on Signal and Information Processing*, 2013, pp. 727–730.

[20] X. Yu, J. Zhang, M. Haenggi, and K. B. Letaief, "Coverage Analysis for Millimeter Wave Networks: The Impact of Directional Antenna Arrays," *IEEE Journal on Selected Areas in Communications*, vol. 35, no. 7, pp. 1498–1512, 2017.

[21] Z. Chen and Y. Zhong, "Characterizing Stability Regions in Wireless Networks With Hard-Core Spatial Constraints," *IEEE Wireless Communications Letters*, vol. 13, no. 8, pp. 2180–2184, 2024.

[22] M. Haenggi, "Mean Interference in Hard-Core Wireless Networks," *IEEE Communications Letters*, vol. 15, no. 8, pp. 792–794, 2011.

[23] H. Q. Nguyen, F. Baccelli, and D. Kofman, "A Stochastic Geometry Analysis of Dense IEEE 802.11 Networks," in *IEEE INFOCOM 2007 - 26th IEEE International Conference on Computer Communications*, 2007, pp. 1199–1207.

[24] Y. Zhong, Z. Chen, W. Zhang, and M. Haenggi, "Dual-zone hard-core model for rts/cts handshake analysis in wlans," *IEEE Transactions on Wireless Communications*, vol. 24, no. 11, pp. 9323–9337, 2025.

[25] Y. Zhong, X. Zhou, and K. Feng, "Spatial network calculus: Toward deterministic wireless networking," *IEEE Transactions on Wireless Communications*, vol. 25, pp. 4707–4720, 2026.

[26] M. Haenggi, "The Mean Interference-to-Signal Ratio and Its Key Role in Cellular and Amorphous Networks," *IEEE Wireless Communications Letters*, vol. 3, no. 6, pp. 597–600, 2014.

[27] R. K. Ganti and M. Haenggi, "Asymptotics and Approximation of the SIR Distribution in General Cellular Networks," *IEEE Transactions on Wireless Communications*, vol. 15, no. 3, pp. 2130–2143, 2016.

[28] S. S. Kalamkar and M. Haenggi, "Simple Approximations of the SIR Meta Distribution in General Cellular Networks," *IEEE Transactions on Communications*, vol. 67, no. 6, pp. 4393–4406, 2019.

[29] M. R. Akdeniz, Y. Liu, M. K. Samimi, S. Sun, S. Rangan, T. S. Rappaport, and E. Erkip, "Millimeter Wave Channel Modeling and Cellular Capacity Evaluation," *IEEE Journal on Selected Areas in Communications*, vol. 32, no. 6, pp. 1164–1179, 2014.